


Mutual interaction of a collapsing bubble and a nearby viscoelastic solid

Jihoo Moon ¹, Ehsan Mahravan ², and Daegyoun Kim ^{1,*}¹*Department of Mechanical Engineering, KAIST, Daejeon 34141, Republic of Korea*²*Department of Mechanical and Production Engineering, Aarhus University, Aarhus 8000, Denmark*

(Received 4 November 2023; accepted 6 March 2024; published 2 April 2024)

The interaction between a microscale collapsing bubble and a nearby viscoelastic solid is investigated numerically. The bubble initiates rapid expansion with high initial pressure, and the stand-off parameter is set to be near 1.0. The viscoelastic properties of the solid are described using the Kelvin-Voigt model, with its elastic modulus E and viscosity η , varying several orders of magnitude ($E = 20\text{--}2000$ kPa and $\eta = 2\text{--}1000$ Pa s). The influence of solid viscoelasticity on bubble behavior and solid deformation are analyzed throughout the entire life cycle of the bubble, from its initial expansion to the moment of liquid jet impingement. The Deborah number, which quantifies the relative timescales of solid deformation and bubble expansion, is employed to characterize the bubble–solid interaction. As the Deborah number increases from the order of 10^{-2} to 10^2 , the dynamics of the bubble converge toward those observed in the cases of a rigid solid; while the solid deformation displacement reduces to a value close to zero, the maximum expansion radius of the bubble increases by up to 8%, and the speed of the liquid jet decreases by approximately 80%. The temporal distribution of energy components within the fluid domain reveals that the maximum expansion radius of the bubble and the kinetic energy of the liquid jet are inversely related to the energy transferred from the fluid to the solid. The imbalance in pressure surrounding the contracting bubble and the narrow region of the liquid jet are responsible for the enhancement of the liquid jet speed for small solid viscosity. Upon the impingement of the liquid jet onto the solid surface, the width and depth of the crater formed by the jet become greater for large jet speed and small solid viscosity.

DOI: [10.1103/PhysRevFluids.9.043603](https://doi.org/10.1103/PhysRevFluids.9.043603)

I. INTRODUCTION

The asymmetric collapse of a gas bubble surrounded by a liquid induces a fast liquid jet. Even a microscale bubble can generate a liquid jet moving at a few hundred meters per second, exerting a large impulse onto nearby structures [1–3]. For this reason, collapsing bubbles and the resultant liquid jets are of great interest in various fields of engineering. For example, the suppression of bubble jets is a crucial issue because of their potential to damage underwater structures and erode their surfaces [4–12]. In biomedical applications, there have been attempts to utilize the directionality and high speed of bubble jets for targeted drug delivery [13–19]. Other engineering applications of bubble jets include printing [20–22] and surface cleaning [23–26].

To take advantage of the features of bubble jets, or to prevent or annihilate their negative effects, it is essential to understand the dynamic behaviors of bubbles near different types of boundaries. Numerous studies have revealed the variations in bubble dynamics in accordance with the properties of proximate boundaries. Blake [27] analytically explained the bubble jet dynamics that occur

*daegyoun@kaist.ac.kr

with different boundaries using the concept of the Kelvin impulse, which successfully predicts the direction of a bubble jet near a rigid solid boundary or free surface. When a bubble collapses near a free surface, the liquid jet is directed away from the free surface [28–31]. By contrast, a bubble that collapses near a rigid surface induces a liquid jet directed towards the rigid surface [32–37]. In both cases, the speed of the liquid jet is primarily determined by the maximum bubble radius and the initial distance between the bubble center and the boundary. Moreover, Supponen *et al.* [38] used an anisotropy parameter to describe the bubble jet dynamics caused by different inducers, such as a free surface or a rigid wall. Using the data reported by previous studies and applying the Kelvin impulse theory, they built an elegant and unified framework that covers the majority of liquid jet dynamics. Several studies have found that different wall geometries such as crevices [39], parallel walls [40], curved walls [41], and mesoscale riblets [42] also play a substantial role in influencing the collapsing behavior of a bubble and the distribution of wall pressure.

Unlike a free surface or a rigid boundary, the case of an elastic surface produces a bubble jet that can be either away from the surface, towards the surface, or even split into two opposite axial directions. These behaviors of a bubble jet near an elastic boundary involve the complex change in bubble morphology and the influence of the elastic boundary. Therefore, the bubble jet dynamics near an elastic surface cannot be predicted simply by the Kelvin impulse theory [43,44], and their characteristics have been identified by various experimental and numerical studies [44–50]. These studies have revealed that the bubble jet dynamics, including the direction and speed of the jet, depend not only on the dimensionless stand-off parameter (the ratio of the initial distance between the bubble center and the boundary to the maximum expansion radius of the bubble) but also on the elasticity of the boundary represented by elastic modulus. When the elastic modulus is relatively small, the collapse of a bubble results in a liquid jet directed away from the boundary. However, a boundary with a high degree of stiffness creates a liquid jet moving towards the boundary. Additionally, an elastic boundary generates a faster liquid jet than a rigid boundary for a broad range of the stand-off parameter [51].

The control of bubble jets near viscoelastic surfaces is an important issue in many applications involving viscoelastic materials, such as *in vivo* drug delivery [52] and histotripsy [53]. In contrast to elastic materials, viscoelastic materials exhibit delayed deformations in response to stress input and release. Incorporating this retardation enables more accurate modeling of a wide range of soft materials, including biological tissues [54], silicones, and polymers [55,56]. While many studies have primarily focused on the effect of the elasticity of a nearby solid surface, relatively few studies have considered surfaces with viscoelastic properties. Early studies done by Shima *et al.* [57] and Duncan *et al.* [58] examined the dynamics of a collapsing bubble near a viscoelastic composite rubber surface. However, the surface was modeled as an elastic solid in the analysis, and thereby the effect of viscoelasticity was not considered. Gong and Klaseboer [59] numerically studied the interaction between a viscoelastic surface and a collapsing bubble, in which circular and rectangular Zener-type viscoelastic plates were used as the boundary. Although changes in the viscosity of the boundary had an insignificant effect on the temporal evolution of the bubble shape, this result was far from being general because only single values were considered for the solid elasticity and stand-off parameter. Rodriguez [60] reported that, for a collapsing bubble near a surface coated with an elastomer made of a Kelvin-Voigt material, both the bubble volume and liquid jet speed decreased as the distance between the bubble and the surface and the thickness of the coating increased. Even in these two studies, parameters such as the standoff distance and the surface thickness were addressed instead of the viscoelasticity. Therefore, it remains unclear how the viscoelastic properties represented by the delay in solid deformation affect the bubble-boundary interactions over the entire lifecycle of a collapsing bubble.

In this paper, we numerically investigate the coupled mechanics between a bubble and a viscoelastic solid surface in an attempt to unravel the salient features of the interactions from the expansion of the bubble to the deformation of the solid following the impact of the liquid jet. The parameters that characterize the viscoelastic properties, namely, the elastic modulus and viscosity, are varied in the Kelvin-Voigt model chosen for the solid. Our numerical model and methods

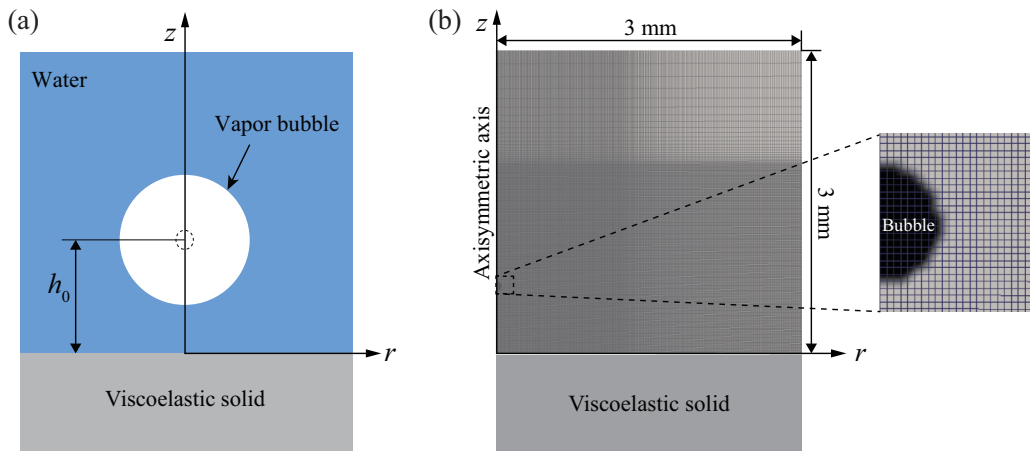


FIG. 1. (a) Schematic of a bubble immersed in water over a viscoelastic solid. (b) Grid layout of axisymmetric two-dimensional fluid domain.

are described in Sec. II. In Sec. III, the bubble dynamics and solid deformation are discussed in sequential order: First, the expansion of the bubble and initial deformation of the solid (Sec. III A); second, the rebound of the solid and contraction of the bubble (Sec. III B); third, the collapse of the bubble and formation of the liquid jet (Sec. III C); and fourth, the deformation of the solid by the liquid jet (Sec. III D). Finally, our findings are summarized in Sec. IV.

II. PROBLEM DESCRIPTION

A. Model and parameters

Initially, a vapor bubble with a radius of $R_0 = 50 \mu\text{m}$ and a high internal pressure of $p_{g,0} = 1.32 \times 10^8 \text{ Pa} = 1300 \text{ atm}$ is surrounded by water at atmospheric pressure and is positioned directly above a viscoelastic solid [Fig. 1(a)]. The distance from the center of the bubble to the flat surface of the solid is set to $h_0 = 660 \mu\text{m}$. Under these conditions, the bubble expands to have a maximum radius of 620–670 μm , depending on solid properties. This sub-micrometer scale is similar to the setups used in previous studies that explored the interaction between bubbles and solid boundaries with various characteristics [5, 14, 34, 37, 47]. Moreover, this length scale is relevant to the collapse of bubbles near biological tissues for *in vivo* drug delivery although the bubbles employed *in vivo* are generally smaller than the bubble of our numerical setup. To facilitate a strong interaction between the bubble and the solid, the initial height h_0 is chosen to be a value similar to the maximum expansion radius of the bubble. Cases with smaller h_0 , which correspond to wall-attached bubbles, are not included in the scope of this paper because the current numerical algorithm for the fluid-solid interaction becomes highly unstable for these cases.

The Kelvin–Voigt model is used as a viscoelastic model for the solid in this paper, as this provides a reasonably simplified constitutive relation for organic tissues [61–63]. This constitutive model consists of one viscous damper and one elastic spring in parallel, and the constitutive equation for three-dimensional deformation is given as

$$\boldsymbol{\sigma} = \lambda(\text{Tr}(\boldsymbol{\epsilon}) + \tau_\lambda \text{Tr}(\dot{\boldsymbol{\epsilon}}))\mathbf{I} + 2G(\boldsymbol{\epsilon} + \tau_S \dot{\boldsymbol{\epsilon}}), \quad (1)$$

where $\boldsymbol{\sigma}$ and $\boldsymbol{\epsilon}$ are stress and strain tensors, respectively. λ is the Lamé's first parameter and G is the Lamé's second parameter or the shear modulus. The Lamé's first parameter λ and the shear modulus G can be calculated from Young's modulus E (termed the elastic modulus in this study)

and Poisson's ratio ν as follows:

$$\lambda = \frac{E\nu}{(1+\nu)(1-2\nu)} \quad \text{and} \quad G = \frac{E}{2(1+\nu)}. \quad (2)$$

τ_λ and τ_S in Eq. (1) are the characteristic times which are normally determined by experiments. The full derivation and detailed explanation of Eq. (1) can be found in Lemaitre and Chaboche [64]. For the numerical Kelvin-Voigt model used in this paper, each value is set to be $\tau_\lambda = 3\eta/E$ and $\tau_S = \eta/G$, where η is the shear viscosity of the solid [65]. The choice of τ_λ and τ_S is justified by the comparison with an analytical solution in Appendix B. The Kelvin-Voigt model is a linear viscoelastic model, and the maximum strain of the solid until the collapse of the bubble is within 10% in this study. Therefore, one should be aware that for materials exhibiting nonlinear viscoelastic behaviors within this strain range, different results may arise.

In all cases, the density and Poisson's ratio of the solid are set to be 1100 kg/m^3 and 0.4, respectively. Five values of $E = [20, 100, 200, 1000, 2000]$ kPa and five values of $\eta = [2, 5, 10, 100, 1000]$ Pa s are considered. These values of the solid properties are arbitrarily selected within the range corresponding to various kinds of human tissue [63,66–69]. Additionally, a rigid solid and five purely elastic solids with different elastic moduli are included for comparison with the viscoelastic solid cases.

B. Fluid solver

A revised OPENFOAM code [70] is used to solve the mass and momentum conservation equations for the multiphase compressible flow of a Newtonian fluid in an axisymmetric two-dimensional domain [Fig. 1(b)]. To reduce computational cost, a two-dimensional domain is adopted under the assumption that the fluid flow and solid deformation are axisymmetric. The axisymmetric condition in bubble collapse simulations can be justified by the results of experimental studies [32,34,43]. Also, this condition has been frequently employed in numerical studies [22,31,37,71],

$$\frac{\partial \rho}{\partial t} + \nabla \cdot (\rho \mathbf{U}) = 0, \quad (3a)$$

$$\frac{\partial(\rho \mathbf{U})}{\partial t} + \nabla \cdot (\rho \mathbf{U} \mathbf{U}) = -\nabla p + \rho \mathbf{g} + \nabla \cdot \boldsymbol{\tau} + \mathbf{f}_s, \quad (3b)$$

where ρ is the fluid density, \mathbf{U} is the fluid velocity, p is the pressure, \mathbf{g} is the gravitational acceleration, $\boldsymbol{\tau}$ is the viscous stress tensor, and \mathbf{f}_s is the surface tension force per unit volume. Note that the bulk viscosity of the fluid is assumed to be zero when accounting for the viscous stress tensor. On the two edges of the fluid domain, one of the following two boundary conditions is applied, depending on the flow direction, for a nonreflective boundary: zero velocity-gradient condition when the flow is outward from the domain and zero velocity condition when there is an inward flow.

To capture the interface between the gas and the liquid, the volume-of-fluid method is employed [71,72],

$$\frac{\partial \alpha}{\partial t} + \nabla \cdot (\alpha \mathbf{U}) + \nabla \cdot (\alpha(1-\alpha) \mathbf{U}_r) = \alpha(1-\alpha) \left(\frac{\psi_g}{\rho_g} - \frac{\psi_l}{\rho_l} \right) \frac{Dp}{Dt} + \alpha \nabla \cdot \mathbf{U}, \quad (4)$$

where α denotes the volume fraction of the liquid phase, which ranges from 0–1. ψ_g and ψ_l are defined as $D\rho_g/Dp_g$ and $D\rho_l/Dp_l$, respectively; the subscripts g and l denote the gas and liquid phases, respectively. \mathbf{U}_r denotes the relative velocity between the gas and the liquid [73].

At the interface, the effective density and viscosity for solving the mass and momentum conservation equations [Eq. (3)] are calculated as

$$\rho = \alpha \rho_l + (1-\alpha) \rho_g \quad \text{and} \quad \mu = \alpha \mu_l + (1-\alpha) \mu_g. \quad (5)$$

The surface tension force f_s in Eq. (3b) is calculated by the continuum surface force model [74], using

$$f_s = -\Upsilon\kappa\nabla\alpha, \quad (6)$$

where Υ is the surface tension coefficient and κ is the curvature of the gas–liquid interface, determined from

$$\kappa = -\nabla \cdot \left(\frac{\nabla\alpha}{|\nabla\alpha|} \right). \quad (7)$$

The phase change between the gas and the liquid is not considered in this paper because it does not play a significant role when the bubble collapses violently in a short duration [75].

For the solution in the transient state, the PISO algorithm is employed [76]. In each iteration, the volume fraction α is calculated before the main PISO algorithm, including the computations of the momentum equation, pressure equation, and corrections, is executed. For spatial discretization, the second-order linear scheme is used for gradient terms, Laplacian terms, the divergence of the deviatoric part of the viscous stress tensor, and the interpolations of values between cell centers. The second-order van Leer scheme is used for the remaining divergence terms. The backward Euler method is used for time marching to ensure numerical stability for shock wave propagation and fluid-solid coupling. The first-order accuracy of the scheme is complemented by the very small time step of the fluid solver, as mentioned in Sec. II C.

The vapor bubble is assumed to be isentropic, neglecting the effect of temperature on vapor density. This assumption is based on the rapid expansion and collapse of the bubble within a very short time, allowing us to neglect the influence of heat exchange between the bubble and the surrounding liquid [31,37,71,77],

$$\frac{p_g}{\rho_g^{\gamma_{\text{isen}}}} = \frac{p_{g,\text{ref}}}{\rho_{g,\text{ref}}^{\gamma_{\text{isen}}}} = \text{const}, \quad (8)$$

where γ_{isen} is the ratio of specific heats ($\gamma_{\text{isen}} = 1.33$). The reference values are the vapor pressure and density at 100 °C, which are $p_{g,\text{ref}} = 1.01 \times 10^5$ Pa and $\rho_{g,\text{ref}} = 0.6$ kg/m³, respectively. The Tait equation of state, written in the form

$$\frac{p_l + B}{\rho_l^{\gamma_{\text{Tait}}}} = \frac{p_{l,\text{ref}} + B}{\rho_{l,\text{ref}}^{\gamma_{\text{Tait}}}} = \text{const}, \quad (9)$$

is used for water. The reference values and coefficients of the equation are $p_{l,\text{ref}} = 1.01 \times 10^5$ Pa, $\rho_{l,\text{ref}} = 998.21$ kg/m³, $\gamma_{\text{Tait}} = 7.15$, and $B = 3.05 \times 10^8$ Pa. The surface tension coefficient is constant as $\Upsilon = 0.073$ N/m.

The two-dimensional axisymmetric fluid domain is a square with side lengths of 3 mm in both the radial (r) and axial (z) directions, and the initial bubble center is located on the z axis above the solid surface [Fig. 1(b)]. For the fluid domain, rectangular and nonuniform 350×350 grids are constructed. Along the r direction, 60% of the grid cells are uniformly distributed in 40% of the domain length from the left side. The remaining 40% of the grid cells have a growth rate of 1.1. Along the z direction, 93% of the grid cells are uniformly distributed in 62% of the domain lengths from the bottom, and the remaining 7% of grid cells have a growth rate of 1.14.

C. Coupling of fluid and solid solvers

The deformation of a viscoelastic surface is simulated using the finite element method. The code is a revised version of CALCULIX [78]. The solid domain is set to be axisymmetric and two-dimensional with dimensions of 3 mm \times 1 mm. For the solid domain, rectangular and uniform 350×50 grids are constructed, and four-node axisymmetric bilinear CAX4 solid elements are used for the discretization. The bottom and side boundaries of the solid domain are fixed, and the top

boundary is allowed to deform according to the interaction with the fluid domain. The validation of the solid solver and the Kelvin–Voigt model is described in Appendix B.

The fluid solver and solid solver are coupled such that they exchange data with each other. We modified the source code of preCICE [79], an open-source library for fluid-structure interaction simulations, for the coupling of the two solvers. Once the flow field has been computed, the pressure data of cell centers located at the bottom of the fluid domain are transferred to the top nodes of the solid domain. When transferring the pressure data, the viscous stress is neglected because its magnitude is much smaller than the stagnation pressure [80] and thereby hardly affects the solid deformation during the growth and collapse of a bubble, which is the main scope of this paper. During data transfer, linear interpolations are performed between the fluid cell centers and the solid nodes if their arrangements do not match. The solid solver then computes the deformation of the solid. Next, the coupling code uses the displacement of the top of the solid to calculate the velocity of the bottom of the fluid domain for the following coupled iteration.

For the coupling code and the solid solver, each time step is fixed at 2×10^{-9} s. For the fluid solver, an additional condition is imposed for the time step, limiting the maximum Courant number to 0.2. This is because flow phenomena in the fluid domain, such as shock waves, involve dramatic changes in physical properties. The time step can be adjusted during runtime to satisfy that the Courant number does not exceed 0.2 and to ensure the accuracy of the simulation. Therefore, for each coupled iteration, the fluid solver performs multiple sub-cycles if the time step size is below 2×10^{-9} s. On the other hand, the time step size of 2×10^{-9} s is sufficiently small for the solid solver. The highest wave propagation speed in the solid, $c = (E/\rho_s)^{1/2}$, is calculated to be 44 m/s when the elastic modulus E is 2000 kPa. The length of the smaller side of a single cell in the solid domain, Δx_s , is 8.5×10^{-3} mm. The maximum Courant number in the solid domain is thereby calculated to be $c\Delta t/\Delta x_s \approx 0.01$. For the fluid-solid coupling, such a small time step guarantees numerical stability and accuracy near the fluid-solid interface.

D. Grid convergence test and validation

To ensure that the simulation results are independent of grid resolution, a grid convergence test is performed for a viscoelastic case ($E = 1000$ kPa, $\eta = 10$ Pa s) by varying the numbers of grid points, N , along each side of the fluid domain; the cell size is inversely proportional to N . While the maximum radius R_{\max} of the expanding bubble increases as N increases from 69 to 156, it exhibits little variation when $N \geq 350$, with a percentage difference of less than 0.1% [Fig. 2(a)]. When the bubble expands in a nonspherical form, the bubble radius R is defined as half the distance between the topmost and bottommost locations of the bubble. The maximum downward displacement δ_{\max} of the solid surface at $r = 0$ during the bubble expansion has an error of less than 0.5% relative to the $N = 350$ case when $N \geq 350$ [Fig. 2(b)]. For a time-resolved comparison, the time histories of pressure at the center of the solid surface, p_c , are shown in Fig. 2(c). The differences in p_c between the cases of $N \geq 350$ are negligible. These results confirm that grid independence is achieved in both the fluid and solid domains by using grids with $N = 350$.

To validate our fluid solver, simulation results are compared with the experimental results of Ma *et al.* [43] for a bubble expanding near a rigid solid surface with the stand-off parameter $\gamma = 1.56$ [Fig. 3(a)]. In the simulation, the initial radius of the bubble is set as $120 \mu\text{m}$ by trial and error to match the experimental condition. The temporal changes in the positions of the topmost and bottommost parts of the bubble in the simulation agree well with those of the experiment, which ensures that the fluid solver accurately predicts the actual behavior of a bubble. The fluid solver can also accurately calculate shock waves induced by the sudden expansion of a bubble. A detailed validation for the accuracy of shock capturing is presented in Appendix A.

For the validation of our fluid-structure coupling algorithm, numerical simulations of a collapsing bubble near an elastic solid are conducted. The values of the elastic modulus, stand-off parameter, and maximum expansion radius for the simulations are set to be those of the experiments by Brujan *et al.* [51]. The simulation results are compared with the image frames from Brujan *et al.* [51]

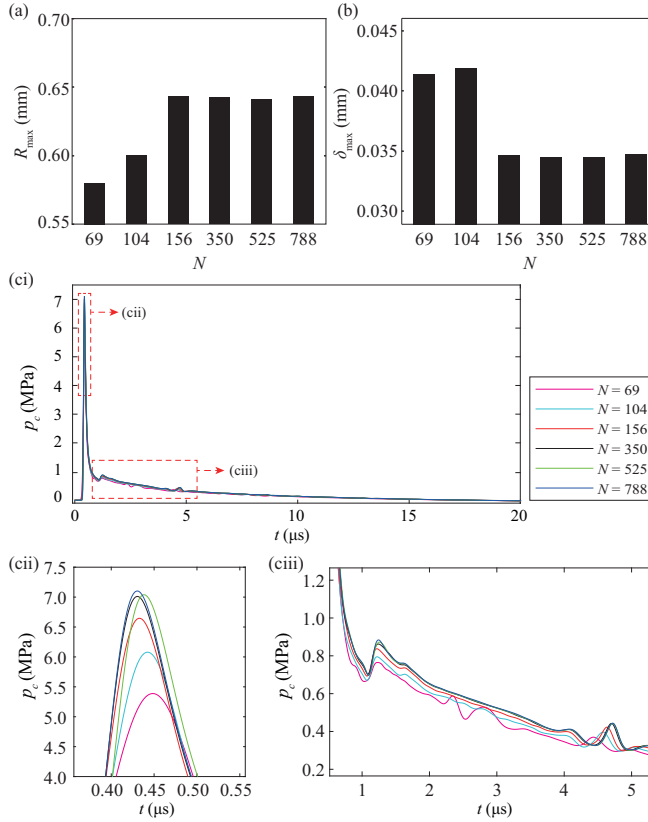


FIG. 2. Grid convergence test results for (a) maximum radius R_{\max} of the expanding bubble near a viscoelastic solid ($E = 1000$ kPa, $\eta = 10$ Pa s) and (b) maximum downward displacement δ_{\max} of the viscoelastic solid during bubble expansion. (c) Temporal change in pressure at solid center, p_c , for different grid sizes; the graph is zoomed in for the moments (cii) when the shock wave reaches the solid surface and (ciii) when the bubble expands above the surface. The number of grid points $N = 69$ –788.

[Fig. 3(b)]. The shapes of a bubble during its growth and shrinkage are very similar between the experiments and our simulations. The simulation can also successfully capture the intricate effect of the solid elasticity and stand-off parameter on the jetting behavior. If the solid elasticity is absent, the two bubbles shown in Figs. 3(bi) and 3(bii) should generate liquid jets directing towards the solid surface. In the simulations, the deformation of the solids due to the pressure exerted by the fluid motion is accurately computed. As a result, it is possible to produce a split jet [Fig. 3(bi)] and a jet away from the solid boundary [Fig. 3(bii)] through the simulations, which are also observed in the experiments.

At the final frames in Figs. 3(bi) and 3(bii), the sizes of the bubbles are greater to some extent than those of the experiments. This discrepancy in the bubble sizes during the secondary bubble expansion is attributed to neglecting phase change between gas and liquid as previously reported by Zeng *et al.* [37]. Although this issue can be resolved by artificially increasing the polytropic exponent of the gas right after the first bubble collapse [37], our simulations are conducted without such numerical technique because the scope of this paper is confined to the first expansion and collapse phases for a bubble. Also, a nonlinear deformation behavior of the polyacrylamide gel used in the experiments of Brujan *et al.* [51] might be one of the reasons for the small differences in bubble shapes because the simulations employ the linear elastic model for validation. In summary,

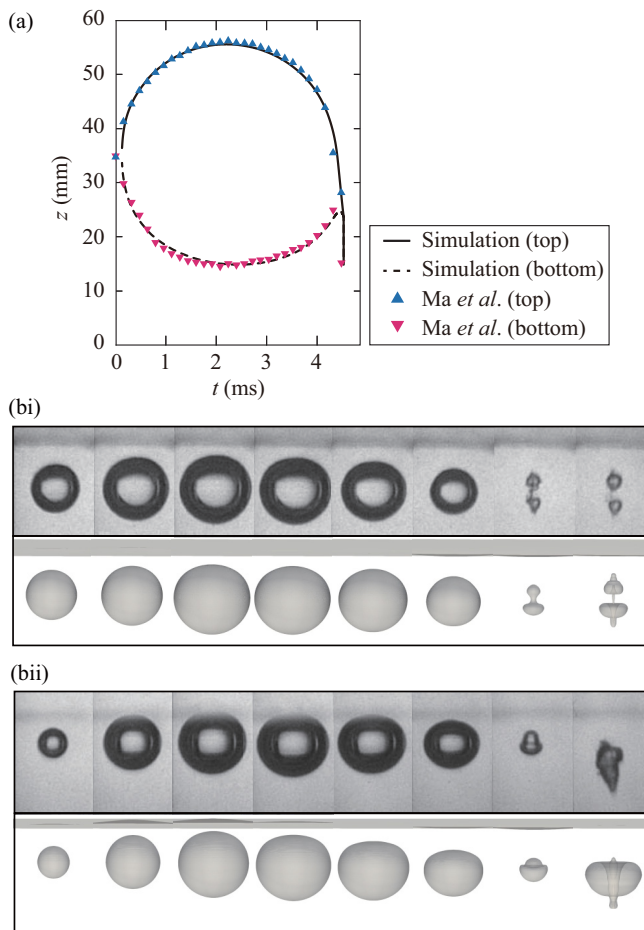


FIG. 3. (a) Comparison of bubble evolution near a rigid solid between experiment [43] and simulation. (b) Comparisons of bubble evolution near an elastic solid between experiments [51] (upper) and simulations (lower): (i) $E = 124$ kPa, $\gamma = 0.87$; (ii) $E = 1040$ kPa, $\gamma = 1.22$. Frame interval is $40 \mu\text{s}$, and frame width is 3.5 mm.

the fluid-structure coupling algorithm used in this paper can reliably compute the interaction of a bubble with a deformable solid for the phases of our interest. In addition to the elastic model, the Kelvin-Voigt viscoelastic model is adopted in our simulations, and the deformation of this viscoelastic model is rigorously validated in Appendix B.

III. RESULTS AND DISCUSSION

A. Bubble expansion and initial solid deformation

When a bubble starts to expand, the surrounding fluid is radially pushed away and its pressure increases dramatically. The high-pressure fluid is also transported towards the liquid-solid interface, deforming the viscoelastic solid downwards. The magnitude of this initial downward deformation induced by bubble expansion varies by several orders, depending on the solid viscosity, for a given elastic modulus [Fig. 4(a)]. The z coordinate is normalized by the initial distance between the bubble center and solid surface, h_0 , as depicted in Fig. 1(a). As the solid viscosity increases from zero to 1000 Pa s, the magnitude of the maximum deformation of the solid decreases from $z/h_0 = 0.35$ to

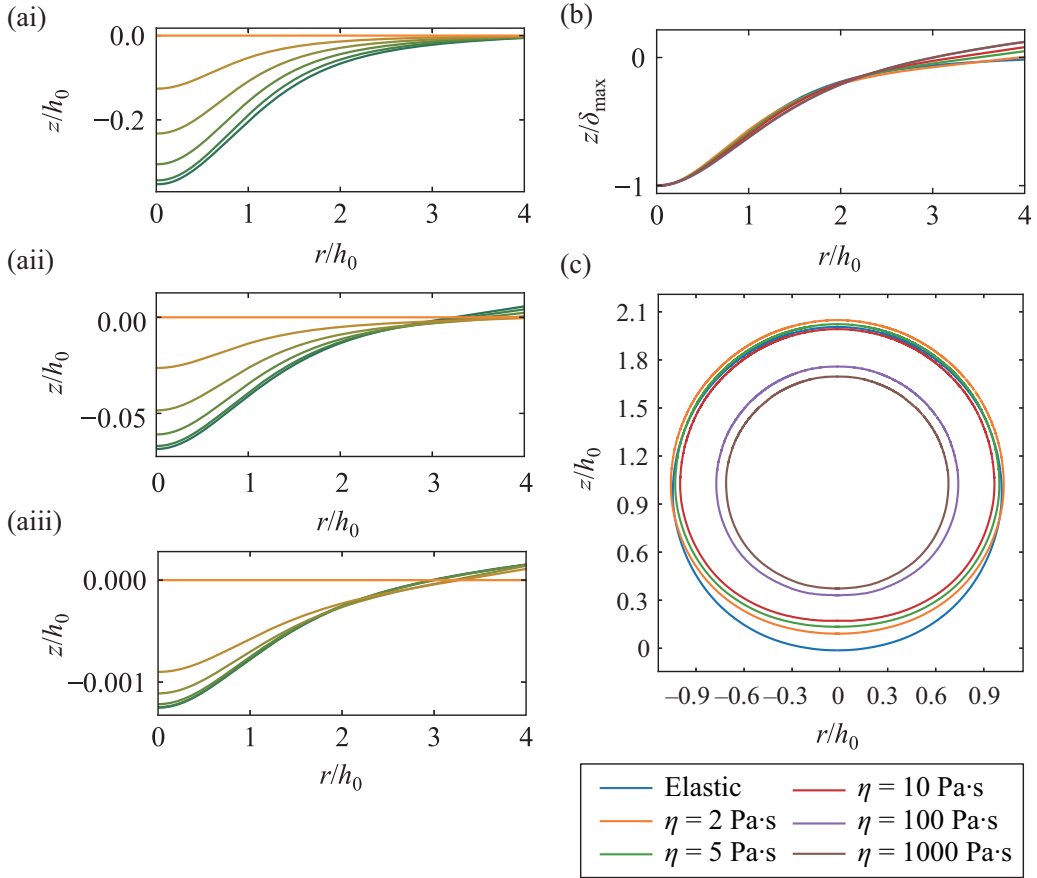


FIG. 4. (a) Sequential profiles of solid surface at initial solid deformation stage: (i) purely elastic, $E = 20$ kPa; (ii) $E = 20$ kPa, $\eta = 10$ Pa·s; (iii) $E = 20$ kPa, $\eta = 1000$ Pa·s. The profiles are captured every $t_{\delta_{\max}}/5$ up to the time corresponding to maximum deformation, $t = t_{\delta_{\max}}$. (b) Surface profiles normalized by maximum displacement δ_{\max} at the solid center and (c) bubble shapes at $t = t_{\delta_{\max}}$ for one elastic case and five viscoelastic cases. All cases have the same elastic modulus, $E = 20$ kPa.

0.0013 at the solid center, $r/h_0 = 0$, for the given elastic modulus of 20 kPa. Throughout this paper, the results for $E = 20$ kPa are mainly used to examine the effects of solid viscosity, because the most noticeable bubble-solid interaction is produced by the smallest elastic modulus and the greatest solid deformation. Since the degree of the solid deformation changes broadly with the solid viscosity, a direct comparison of the surface profiles between the cases is inappropriate. Instead, each profile at the instant of maximum deformation is normalized with its maximum deformation length from the initial horizontal surface, δ_{\max} , and illustrated in Fig. 4(b). When the solid surface reaches the state of maximum deformation, the overall normalized deformation profiles of the surface are quite similar in the range $r/h_0 = 0 - 2$, regardless of the viscosity [Fig. 4(b)]. However, with increasing viscosity, the surface in the region of $r/h_0 > 2$ moves upwards from the initial position, having distinct deviations in the profiles.

In viscoelastic cases with $E = 20$ kPa, the bubble center, which is defined as the middle point between the topmost and bottommost points of the bubble, $(z_{\text{top}} + z_{\text{bot}})/2$, is positioned slightly above its initial position at the time corresponding to maximum displacement, $t = t_{\delta_{\max}}$: $1.04 \leq z/h_0 \leq 1.09$ [Fig. 4(c)]. By comparison, the bubble center of the purely elastic case is lower

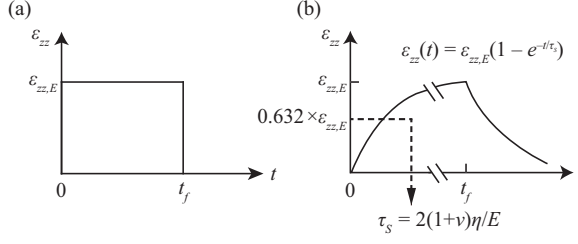


FIG. 5. Temporal strain responses for (a) an elastic material and (b) a Kelvin–Voigt material under constant stress.

($z/h_0 = 1.00$) than in the viscoelastic cases because the downward deformation of the solid is much greater. The bubble size at $t = t_{\delta_{\max}}$ decreases monotonically with increasing viscosity because the solid reaches its maximum deformation sooner when the viscosity is greater.

In Eq. (1), the two parameters that describe the behavior of the Kelvin–Voigt model are the shear modulus $G = E/(2(1 + \nu))$ and shear viscosity η of the solid. If a constant stress $\sigma_{zz,0}$ is imposed axially on the Kelvin–Voigt material, the characteristic time, $\tau_S (= \eta/G = 2(1 + \nu)\eta/E)$, is the time at which the strain reaches 63.2% of the strain in the purely elastic response, $\epsilon_{zz,E}$ (Fig. 5); also see Appendix B. For a given value of E , τ_S determines how slowly the Kelvin–Voigt material responds to the stress input.

Although this delay in the deformation makes viscoelastic materials distinct from elastic materials, the fluid–structure interaction including a bubble and a viscoelastic solid cannot be sufficiently characterized by τ_S alone. Along with the timescale of the viscoelastic deformation, the representative timescale of the bubble dynamics should also be considered to fully describe the interaction. If τ_S is much greater than the lifecycle of a bubble, the deformation of the solid would be hardly detectable until the bubble grows and collapses. Therefore, it is evident that the bubble dynamics would be very smaller to those of the rigid solid case. On the other hand, if τ_S is very small compared to the life cycle of the bubble, the delay in the solid deformation would be negligible and the overall fluid–structure interaction is expected to be similar to that of the elastic solid case. From this conjecture, we argue that the timescale τ_S of the viscoelastic solid relative to the reference time t_{ref} of the expanding bubble, τ_S/t_{ref} , can be regarded as a representative dimensionless parameter for describing the fluid–structure interaction between the viscoelastic solid and the bubble. This dimensionless parameter actually corresponds to a specific form of the Deborah number De [81]. In this paper, the quantities that characterize the bubble dynamics and solid deformation, such as the speed of the bubble jet and the maximum deformation of the solid, will be analyzed using the Deborah number:

$$De = \frac{\tau_S}{t_{\text{ref}}} = \frac{2(1 + \nu)\eta/E}{t_{\text{ref}}}. \quad (10)$$

In the Deborah number [Eq. (10)], the reference time t_{ref} of the bubble is determined to be the time taken for a bubble in an ambient condition (in the absence of a solid) to reach its maximum radius R_{ref} . Both t_{ref} and R_{ref} in the absence of a solid are obtained by solving the Gilmore equation [82], which is a modified version of the Rayleigh–Plesset equation to consider the compressibility effect, with the fifth-order Runge–Kutta method:

$$R \frac{d^2 R}{dt^2} \left(1 - \frac{1}{c} \frac{dR}{dt} \right) + \frac{3}{2} \left(\frac{d^2 R}{dt^2} \right)^2 \left(1 - \frac{1}{3c} \frac{dR}{dt} \right) = H \left(1 + \frac{1}{c} \frac{dR}{dt} \right) + \frac{R}{c} \frac{dH}{dt} \left(1 - \frac{1}{c} \frac{dR}{dt} \right), \quad (11)$$

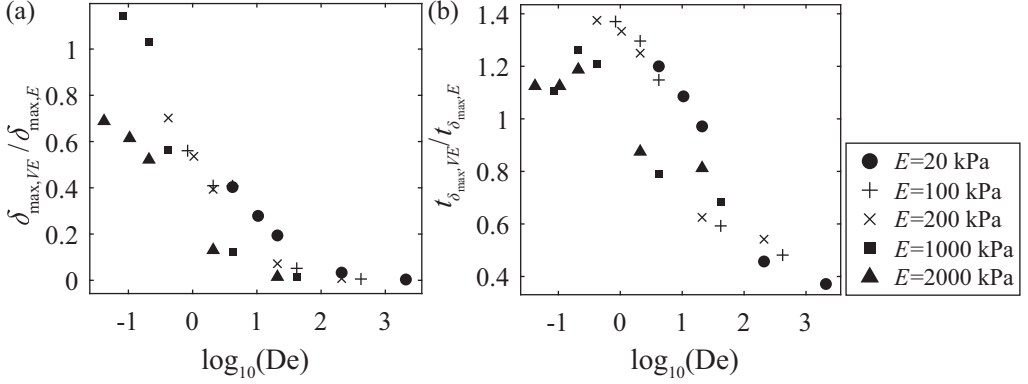


FIG. 6. (a) Normalized maximum displacement $\delta_{\max,VE}/\delta_{\max,E}$ and (b) normalized time at maximum displacement, $t_{\delta_{\max,VE}}/t_{\delta_{\max,E}}$, with respect to the Deborah number De .

where

$$H = \gamma_{\text{Tait}} \left(\frac{p_{\infty} + B}{(\gamma_{\text{Tait}} - 1)\rho_l} \right) \left[\left(\frac{p_l + B}{p_{\infty} + B} \right)^{\frac{\gamma_{\text{Tait}} - 1}{\gamma_{\text{Tait}}}} - 1 \right], \quad (12a)$$

$$c = c_{\infty} \left(\frac{p_l + B}{p_{\infty} + B} \right)^{\frac{\gamma_{\text{Tait}} - 1}{2\gamma_{\text{Tait}}}}, \quad (12b)$$

$$p_g = p_{g,0} \left(\frac{R_0}{R} \right)^{3\gamma_{\text{isen}}} + p_v - \frac{2\Upsilon}{R} - 4\mu_g \frac{1}{R} \frac{dR}{dt}, \quad (12c)$$

$$c_{\infty} = \left[\gamma_{\text{Tait}} \left(\frac{p_{\infty} + B}{\rho_l} \right) \right]^{\frac{1}{2}}. \quad (12d)$$

p_{∞} is the far field pressure, $p_v (=3.17 \times 10^3 \text{ Pa})$ is the vapor pressure of water, and R_0 is the initial radius of the bubble. The pressure inside the bubble is calculated from the radius R of the bubble, assuming isentropic expansion. From the initial conditions considered in this paper, the solution of Eq. (11) is $t_{\text{ref}} = 66.6 \mu\text{s}$ and $R_{\text{ref}} = 0.71 \text{ mm}$, which are consistent with the simulation result using our fluid solver: $65.0 \mu\text{s}$ and 0.72 mm , respectively.

Figure 6 presents the maximum displacement δ_{\max} of the solid and the corresponding time $t_{\delta_{\max}}$ with respect to the Deborah number De . The values of δ_{\max} and $t_{\delta_{\max}}$ for the viscoelastic solids are normalized by those of the elastic solid with an identical elastic modulus, respectively. This provides a better understanding of the effects of solid viscosity on δ_{\max} and $t_{\delta_{\max}}$ in comparison with the purely elastic solid. The subscripts VE and E denote viscoelastic and elastic solids, respectively. Both $\delta_{\max,VE}/\delta_{\max,E}$ and $t_{\delta_{\max,VE}}/t_{\delta_{\max,E}}$ have an inverse relationship with De . That is, a viscoelastic solid with a greater characteristic time $\tau_s (=2(1+\nu)/E)$ exhibits a weaker response to bubble expansion, which is consistent with the preceding statement associated with Fig. 5(b) regarding the general property of the Kelvin-Voigt material. For the discussion of the dimensional δ_{\max} and $t_{\delta_{\max}}$ with respect to the solid viscosity η , readers are referred to Appendix C.

B. Surface rebound and bubble contraction

The downward displacement of the solid reaches its maximum value before the bubble has fully expanded. Thus, the dynamics of the solid can be divided into two stages before the full expansion of the bubble: subsidence before the maximum deformation and rebound after the maximum

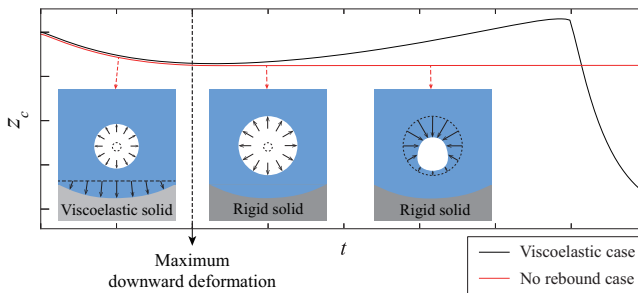


FIG. 7. Graphical description of the special numerical simulation. A viscoelastic solid with $E = 100$ kPa and $\eta = 2$ Pa s is switched to a rigid solid after it reaches the maximum downward deformation (vertical dashed line). z_c is the z coordinate of the solid surface center.

deformation. To determine which of these stages is the dominant influence on the full expansion and subsequent collapse of a bubble, a special numerical simulation was conducted, where the solid was artificially prescribed to stop rebounding after reaching its maximum downward deformation (Fig. 7). Although such behavior is physically infeasible, this artificial method is a straightforward and intuitive means of removing the effect of solid rebound and solely considering the effect of solid subsidence.

The normalized parameters of the bubble, which characterize the bubble expansion (R_{\max} and $t_{R_{\max}}$) and jet formation after bubble collapse (U_j and t_{collapse}), are compared in Table I for three different cases: the normal viscoelastic case, the viscoelastic case where the rebound of the solid is artificially paused after maximum deformation, and the rigid solid case. R_{\max} is the maximum radius of the bubble at full expansion and $t_{R_{\max}}$ is the time corresponding to the full expansion phase; the bubble radius is defined as half the distance between the topmost and bottommost points of the bubble. U_j and t_{collapse} will be discussed later in Sec. III C. U_j is normalized by $U_0 (= ((p_\infty - p_v)/\rho_l)^{\frac{1}{2}} = 9.92 \text{ ms}^{-1})$, where $p_\infty (= 1.01 \times 10^5 \text{ Pa})$ is the far-field pressure and $p_v (= 3.17 \times 10^3 \text{ Pa})$ is the vapor pressure of water. R_{\max} and $t_{R_{\max}}$ differ in the normal and no-rebound cases because the bubble can continue to expand even after the beginning of solid rebound. If the solid rebound is prohibited, the parameter values in Table I change significantly from those of the normal case and become rather closer to those of the rigid solid. This indicates that the rebound of the solid affects the full expansion and contraction of the bubble more strongly than its subsidence.

The change in the maximum expansion radius R_{\max} is not always monotonic with respect to elasticity or viscosity [Fig. 8(a)]. For a large E ($E \geq 1000$ kPa), R_{\max} increases with η . However, for $E \leq 100$ kPa, the trend is no longer monotonic: R_{\max} drops as η increases from 2 Pa s to 10 Pa s, and then rises when $\eta > 10$ Pa s. Furthermore, while E has a negligible influence on R_{\max} at large viscosity ($\eta \geq 100$ Pa s), the variations in R_{\max} with respect to E become remarkable in the small-viscosity range ($\eta \leq 10$ Pa s), and the cases with small E tend to produce larger R_{\max} . Large

TABLE I. Comparison of major parameters characterizing bubble expansion and bubble jet formation between three cases: normal viscoelastic solid, viscoelastic solid with no rebound, and rigid solid. For both the normal and no-rebound cases, the viscoelastic properties are $E = 100$ kPa and $\eta = 2$ Pa s.

	Normal	No rebound	Rigid
R_{\max}/R_{ref}	0.83	0.88	0.89
$t_{R_{\max}}/t_{\text{ref}}$	0.80	0.91	0.96
U_j/U_0	21.06	10.43	8.48
$t_{\text{collapse}}/t_{\text{ref}}$	1.65	1.80	1.92

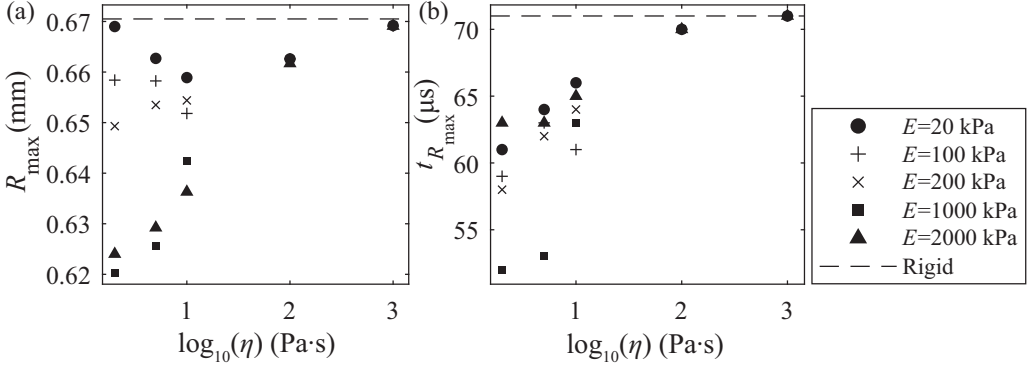


FIG. 8. (a) Maximum expansion radius R_{\max} and (b) time at maximum expansion, $t_{R_{\max}}$, of the bubble for different solid properties.

values of R_{\max} produced by a small elastic modulus and viscosity (i.e., $E = 20$ kPa, $\eta \leq 10$ Pa s) can be explained by the huge compliance of the solid, as reported in Fig. 19(a) of Appendix C. The initial downward deformation of the solid changes the pressure distribution of the water around the bubble, indirectly affecting the expansion of the bubble. Compared with the rigid solid, which acts only as a restriction that keeps the lower side of the bubble from expanding, the downward displacement of the deformable solid allows more space for bubble expansion. For a fixed viscosity, R_{\max} approaches that of the rigid solid case when the elastic modulus increases because the solid deforms less.

Similar to R_{\max} , the time at which maximum expansion occurs, $t_{R_{\max}}$, tends to increase and approaches that of the rigid solid as the viscosity increases [Fig. 8(b)]. The variations in $t_{R_{\max}}$ with respect to E are also negligible at large viscosity ($\eta \geq 100$ Pa s). However, in contrast to R_{\max} , it is difficult to identify any clear relationship between $t_{R_{\max}}$ and E at smaller viscosities ($\eta \leq 10$ Pa s).

As can be seen from Fig. 8(a) and Ref. [19], R_{\max} exhibits no correlation with the parameters relevant to solid deformation, δ_{\max} and $t_{\delta_{\max}}$. To further investigate the change in R_{\max} with respect to these solid properties, a quantitative analysis of the energy components in the fluid and solid domains is conducted. The energy present in the fluid domain can be largely categorized as the kinetic energy of the gas and liquid, E_K , and the potential energy of the bubble, E_P . These are calculated as follows [83]:

$$E_K = \int_V \frac{1}{2} \rho |\mathbf{U}|^2 dV, \quad (13a)$$

$$E_P = (p_\infty - p_v)(V_g - V_{g,0}) + \frac{p_{g,0} V_{g,0}}{\gamma_{\text{isen}} - 1} \left(\frac{V_{g,0}}{V_g} \right)^{\gamma_{\text{isen}} - 1} + \Upsilon A_g + (\rho_g - \rho_l) g V_g z_g, \quad (13b)$$

where $|\mathbf{U}|$ is the velocity magnitude of the fluid and V is the entire volume of the fluid. V_g is the volume of the bubble and $V_{g,0}$ is the volume of the bubble at the initial time. A_g is the surface area of the bubble, and z_g is the location of the bubble center with respect to the initial position. The last two terms in Eq. (13b) represent the interfacial energy and gravitational energy of the bubble, respectively. These two terms are negligible as their magnitudes are much smaller than the remaining terms of E_P in Eq. (13b). In all cases, the interfacial energy is approximately 0.1%, and the gravitational energy is only 0.001% of the total value of E_P . The energy loss in the fluid domain is primarily caused by acoustic radiation, including a shock wave, E_R , and energy transfer from the fluid domain to the solid domain, E_S . E_S is calculated on the fluid-solid interface S as

$$E_S = \int_0^t \left(\int_S (-pn) \mathbf{v} dS \right) dt, \quad (14)$$

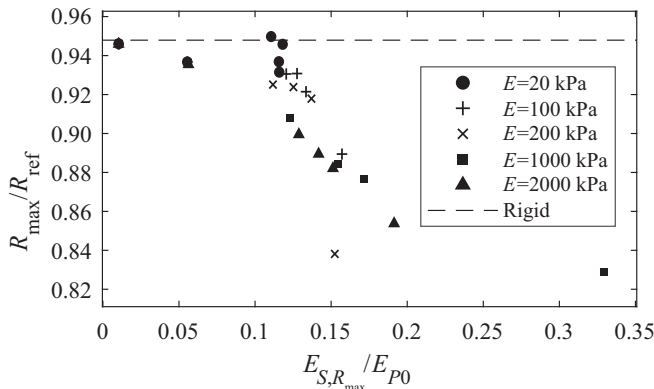


FIG. 9. Dimensionless maximum expansion radius R_{\max}/R_{ref} of the bubble with respect to the dimensionless energy transferred to the solid domain, $E_{S,R_{\max}}/E_{P0}$, up to the maximum expansion phase. The dashed horizontal line denotes the value for the rigid solid case.

where p is the hydrodynamic pressure acting on the solid surface, \mathbf{n} is the unit normal vector on the interface into the fluid domain, and \mathbf{v} is the velocity of the interface. As can be seen from the integration over time in Eq. (14), E_S is the cumulative sum of the energy transferred from the moment of cavitation inception. Hence, this term includes the energy transfer not only by the jet impact but also by the gradual deformation of the interface throughout the entire time.

The potential energy of the bubble at the initial time, E_{P0} , should be balanced by the total energy budget of the fluid domain:

$$E_{P0} = E_K + E_P + E_R + E_S. \quad (15)$$

At the instant of full expansion of the bubble ($t = t_{R_{\max}}$), E_R is almost invariant between all cases because the acoustic energy radiating to the far field is hardly affected by the solid properties. Additionally, when the bubble has fully expanded, the kinetic energy E_K in the fluid domain is almost zero in all cases; the temporal changes in the energy components are discussed later using Fig. 14 in Sec. III C. As the maximum radius R_{\max} is directly related to the potential energy E_P of the bubble, R_{\max} depends on the remaining energy term, which is the total energy transferred to the solid domain, $E_{S,R_{\max}}$, until the bubble reaches its full expansion. Indeed, in Fig. 9, there is an inverse relationship between the normalized parameters R_{\max}/R_{ref} and $E_{S,R_{\max}}/E_{P0}$, albeit there are some deviations in the data points. As the solid domain absorbs more energy from the initial potential energy of the bubble, the bubble grows to a smaller size. Furthermore, in most cases, the maximum radius of the bubble is less than that of the rigid solid case because there is zero energy transfer to the rigid solid: $E_S = 0$. Obviously, the surface deformation becomes greater in cases with smaller elastic modulus and viscosity [Fig. 19(a)]. However, the elastic modulus and viscosity have opposite effects on $E_{S,R_{\max}}$. $E_{S,R_{\max}}$ is generally greater when the solid has a large elastic modulus and a small viscosity (Fig. 9).

As the solid surface rebounds after its maximum downward deformation, the bubble reaches its maximum expansion and begins to contract under a high-pressure field created around the bubble. For a given elastic modulus, a solid with a smaller viscosity (and thus lower De) rebounds a longer distance with a higher speed [Fig. 10(a)]. This longer and faster rebound induces a stronger upward flow above the solid surface and increases the pressure between the surface and the bubble.

The upward flow and pressure increment during the rebound stage produce different contraction behaviors in the bubble [Figs. 10(bi)–10(biii)]. The dependency of the contraction shape on the elastic modulus has already been reported for the interaction with elastic solids [43], and here we affirm that the solid viscosity also affects the contraction shape. For the purely elastic case

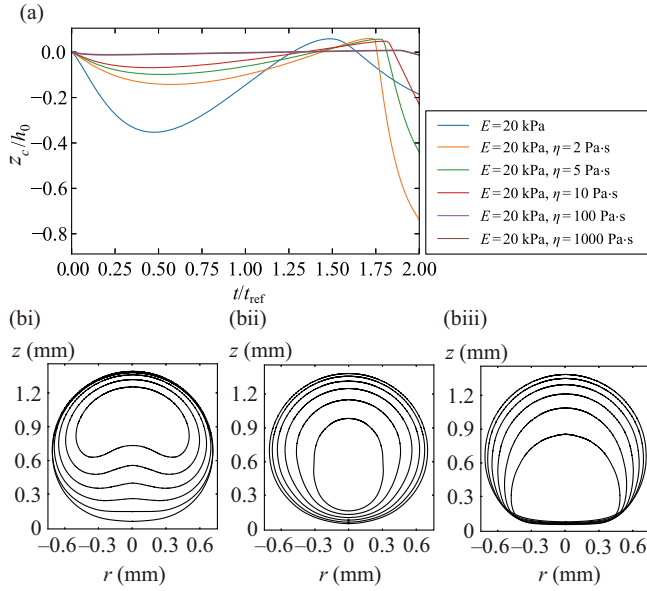


FIG. 10. (a) Temporal change in the z coordinate z_c/h_0 of the solid surface at $r = 0$ for a purely elastic solid and five viscoelastic solids. All cases have the same elastic modulus, $E = 20$ kPa. (b) Evolution of bubble shape during contraction for a purely elastic solid and two viscoelastic solids: (i) purely elastic, $E = 20$ kPa; (ii) $E = 20$ kPa, $\eta = 2$ Pa s; (iii) $E = 20$ kPa, $\eta = 1000$ Pa s.

[Fig. 10(bi)], the surface rebound is much greater and faster than any viscoelastic case, as shown in Fig. 10(a). This is because the elastic strain energy of the solid has no viscous dissipation. Therefore, the lower part of the bubble contracts much faster than its upper part. Regarding the viscoelastic cases [Figs. 10(bii) and 10(biii)], while the overall bubble shape is nearly elliptical with quite symmetric upper and lower parts in the smaller η case, the lower part is almost flat in the larger η case because of the weak surface rebound, leading to distinctly asymmetric upper and lower parts. The curvature radius of the bubble's lower part with the smaller η is less than with the larger η . In Fig. 10(b), three cases with $E = 20$ kPa are chosen to demonstrate how the bubble shape is affected by the solid viscosity. The influence of η on the bubble shapes becomes less distinct as E increases and the solid deformation is weaker.

C. Bubble collapse and liquid jet generation

After contraction, the bubble collapses, creating a fast liquid jet. The notable difference in the contraction shapes of the bubble between the elastic cases and the viscoelastic cases, as exemplified in Figs. 10(bi)–10(biii), leads to different jet directions. In the elastic cases, the jet is directed upwards away from the solid for $E = 20$ and 100 kPa, and splits into upward and downward directions for $E = 200$ kPa or higher [Figs. 11(a)–11(e)]; these results are consistent with the experimental results of Brujan *et al.* [51]. By contrast, the jet created in the viscoelastic cases is directed towards the solid, except in two cases ($E = 1000$ kPa, $\eta = 2$ Pa s and $E = 1000$ kPa, $\eta = 5$ Pa s) [Figs. 11(g)–11(k)]. In the rigid solid case, the jet is directed toward the solid, as expected [Fig. 11(f)].

The speed of the liquid jet is relevant to the degree of damage imposed on the solid surface and also affects the efficient utilization of the jet in applications such as drug delivery and surface cleaning. A single representative value of the liquid jet speed, U_j , is defined as the maximum speed of the liquid jet before the upper part of the bubble surface contacts its lower part. To obtain the exact

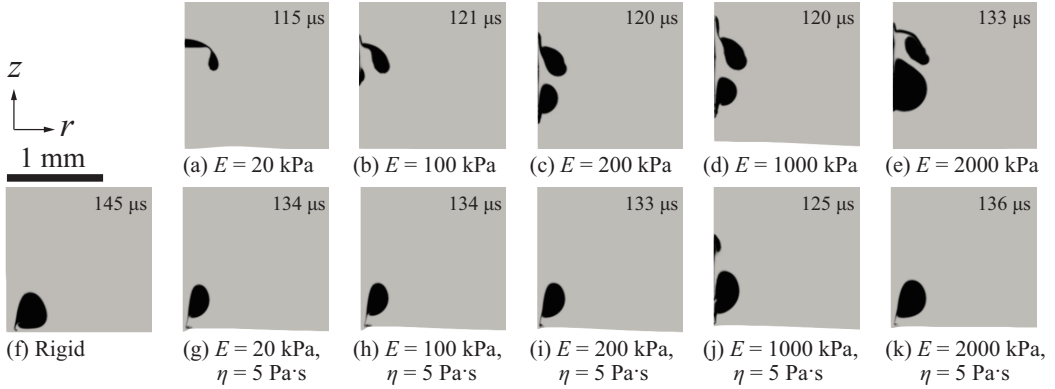


FIG. 11. Formation of liquid jet in elastic solid cases (a)–(e), viscoelastic solid cases (g)–(k), and a rigid solid case (f). Black and grey denote the gas bubble and water areas, respectively. The number on the top right corner of each panel indicates the time at which each case is captured. See Supplemental Material movie 1 [84].

value of U_j , the travel distance Δz of the tip of the liquid jet, the location of which corresponds to the upper part of the bubble interface on the z axis, during a single simulation frame is divided by the frame time ($1 \mu\text{s}$); see the schematic on the right of Fig. 12. The collapse time of the bubble, t_{collapse} , is defined as the time interval from its initial explosion to the instant at which the upper and lower parts of the bubble contact each other just before collapse.

For comparison with the purely elastic solid, U_j and t_{collapse} are normalized by their values in the elastic case with an identical elastic modulus E , respectively, and are presented with respect to the Deborah number De (Fig. 12); the subscripts VE and E denote viscoelastic and elastic cases, respectively. Note that the viscoelastic cases with $E = 20 \text{ kPa}$ are omitted in Fig. 12(a) because of the abnormally low jet speed for the purely elastic solid with $E = 20 \text{ kPa}$; this will be addressed in more detail in Fig. 13. The discussion of the dimensional U_j and t_{collapse} versus the solid viscosity η is also presented in Appendix C. Except for $E = 20 \text{ kPa}$, the liquid jet speeds of the viscoelastic cases are smaller than that of the purely elastic solid with the same elastic modulus, while the bubble collapse times of the viscoelastic cases exceed that of the corresponding purely elastic solid. $U_{j,VE}/U_{j,E}$ exhibits a decreasing trend with increasing De , while $t_{\text{collapse},VE}/t_{\text{collapse},E}$ shows an increasing trend. From Fig. 12, U_j and t_{collapse} are found to be inversely related to each other. Such

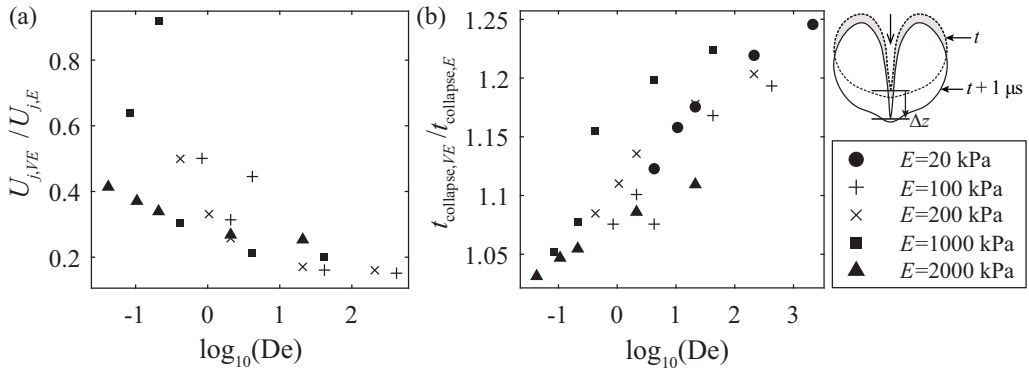


FIG. 12. (a) Normalized liquid jet speed $U_{j,VE}/U_{j,E}$ and (b) normalized bubble collapse time $t_{\text{collapse},VE}/t_{\text{collapse},E}$ with respect to the Deborah number De .

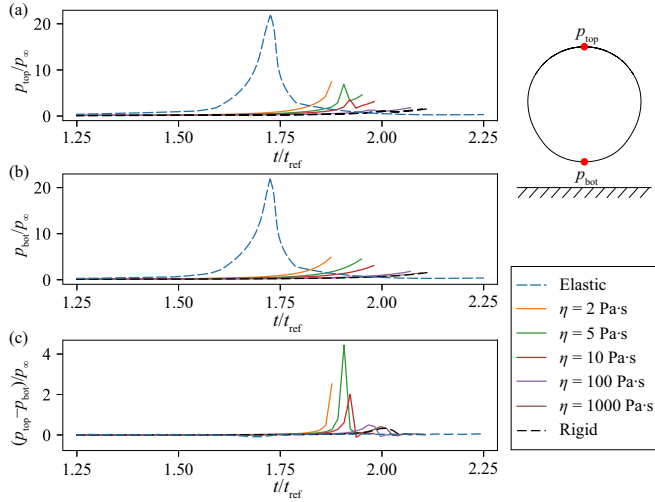


FIG. 13. Temporal change in pressure at (a) topmost point $p_{\text{top}}/p_{\infty}$ and (b) bottommost point $p_{\text{bot}}/p_{\infty}$ of the bubble for different solid properties. (c) Pressure imbalance between the top and bottom points, $(p_{\text{top}} - p_{\text{bot}})/p_{\infty}$. All cases have the same elastic modulus, $E = 20$ kPa.

an inverse relationship between these two variables has been reported with respect to other input parameters, such as the stand-off parameter or the initial pressure of the bubble, under boundary conditions including a flat rigid solid [85] and a curved rigid solid [86]. This is because highly anisotropic pressure around the bubble results in its faster and more violent collapse [38].

The pressure around the bubble throughout its life cycle is now analyzed to reveal how the anisotropic pressure distribution around the bubble affects the jet speed and bubble collapse time. Figures 13(a) and 13(b) illustrate the time history of the pressures acting on the topmost and bottommost points of the bubble, p_{top} and p_{bot} . The pressures are normalized by the far-field pressure p_{∞} , and the time t is normalized by t_{ref} . The pressure imbalance across the bubble, $p_{\text{top}} - p_{\text{bot}}$, begins to grow drastically just before the collapse [Fig. 13(c)]. After the collapse, the curves are cut off at the instant when the bubble forms a toroidal shape because the two points on the z axis used to measure the pressure are no longer available.

For most of the purely elastic solids, the pressure imbalance $p_{\text{top}} - p_{\text{bot}}$ far exceeds that of the viscoelastic solids with an identical elastic modulus during contraction. Accordingly, the jet speed U_j of these purely elastic cases is much greater than that of the viscoelastic cases (Fig. 12). An exception is the value of $p_{\text{top}} - p_{\text{bot}}$ for the purely elastic solid with $E = 20$ kPa, which remains near zero although both p_{top} and p_{bot} are much greater than in the viscoelastic solids (Fig. 13). This case has the smallest elastic modulus among all cases in the present paper and has no viscoelastic damping. Thus, the bubble is least affected by the existence of the solid, and the pressure distribution is highly symmetric at these two points throughout the entire process. Such a low value of $p_{\text{top}} - p_{\text{bot}}$ for $E = 20$ kPa is also responsible for the abnormally low jet speed ($U_j = 122.23$ ms $^{-1}$) and the formation of a relatively blunt upward jet, as shown in Fig. 11(a). For the rest of the elastic cases ($E \geq 100$ kPa), pressure anisotropy is much greater than viscoelastic cases with the same elastic modulus, which is the reason for the high jet speed. For viscoelastic solids, with decreasing η , the peak value of $p_{\text{top}} - p_{\text{bot}}$ generally increases and occurs at an earlier time [Fig. 13(c)]. The stronger pressure anisotropy in the case of lower η leads to a higher liquid jet speed and faster bubble collapse [Fig. 12].

To elicit a deeper understanding of the liquid jet speed, we consider the energy components (E_P , E_K , E_S) introduced in Eq. (15) up to the collapse time of the bubble. The overall trend of $E_{\text{sum}} (= E_P + E_K + E_S)$, E_P , and E_K in the rigid solid case [Fig. 14(c)] is in good agreement with

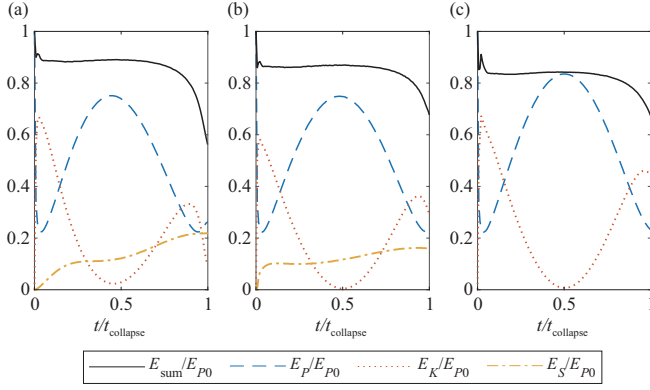


FIG. 14. Temporal change in energy components normalized by initial potential energy E_{P0} of the bubble for different solid properties: (a) purely elastic solid with $E = 20$ kPa; (b) viscoelastic solid with $E = 20$ kPa and $\eta = 10$ Pa s; (c) rigid solid. Time t along the x axis is normalized by the collapse time t_{collapse} .

the results reported by Wang [83]; $E_S = 0$ for the rigid solid. In all three cases shown in Fig. 14, the energy sum E_{sum} suddenly drops by approximately 15% upon the emission of a shock wave right after the initial explosion. Note that E_{sum} in Eq. (15) does not include E_R . E_{sum} then remains almost constant before dropping again near the collapse time, because the amount of acoustic radiation is negligible after the shock wave and no energy other than E_S exits the fluid domain. The potential energy E_P of the bubble suddenly drops after its inception because of rapid loss of its potential energy in the form of a shock wave. Then, the potential energy increases until $t/t_{\text{collapse}} \approx 0.5$, which is the time at which the bubble attains its full expansion, and decreases almost symmetrically afterwards in the contraction phase. Because the potential energy of the bubble is heavily dependent on the bubble volume, the change in E_P over time is quite similar to the change in the bubble volume over time. By contrast, the trend in fluid kinematic energy E_K over time is the opposite to that of E_P . Near $t = 0$, the sudden burst of the bubble and the creation of the shock wave elevate the kinetic energy in the fluid domain. A very short time delay exists between the decrease in E_P and the increase in E_K due to the compressibility effect of the liquid, which may be responsible for the occurrence of a minor spike in E_{sum} . When the bubble reaches the maximum expansion, it remains almost stationary, and thereby the fluid kinetic energy is nearly zero. As the bubble collapses, the bubble interface and the surrounding water undergo violent movement, and thus the fluid kinetic energy at this instant is elevated to its second peak.

As explained in Sec. III B, some of the energy is transferred from the fluid domain to the solid domain through the deformation of the solid; the total energy transferred up to a certain time is denoted as E_S . During the initial explosion, E_S increases steeply and continues to increase thereafter with a lower growth rate during the expansion and contraction phases [Figs. 14(a) and 14(b)]. Although both E_K and E_S increase during the contraction phase, the kinetic energy of the fluid at the instant of bubble collapse, $E_{K,\text{collapse}}$, has an inverse relationship with the total energy transferred to the solid domain up to the time of bubble collapse, $E_{S,\text{collapse}}$, for viscoelastic solids [Fig. 15(a)].

At the bubble collapse time, more than 95% of the kinetic energy in the whole fluid domain is concentrated in the narrow liquid jet region. Therefore, $E_{K,\text{collapse}}$ can be approximated as the kinetic energy of the liquid jet. Interestingly, the liquid jet speed U_j reduces as $E_{K,\text{collapse}}$ becomes greater [Fig. 15(b)]. A liquid jet with a higher U_j is relatively narrow compared with a slower liquid jet, as illustrated by the three examples in Fig. 15(c), and thus has a smaller $E_{K,\text{collapse}}$. In the figure, the dark grey and black regions correspond to the downward liquid jet. The liquid jet speed in Fig. 15(ciii) is roughly three times that in Fig. 15(ci); $U_j/U_0 = 8.77, 13.80,$ and 29.10 for Figs. 15(ci)–15(ciii), respectively. However, the kinetic energy of Fig. 15(ciii) is much smaller because the jet itself is much thinner; $E_{K,\text{collapse}}/E_{P0} = 0.44, 0.29,$ and 0.16 for Figs. 15(ci)–15(ciii), respectively.

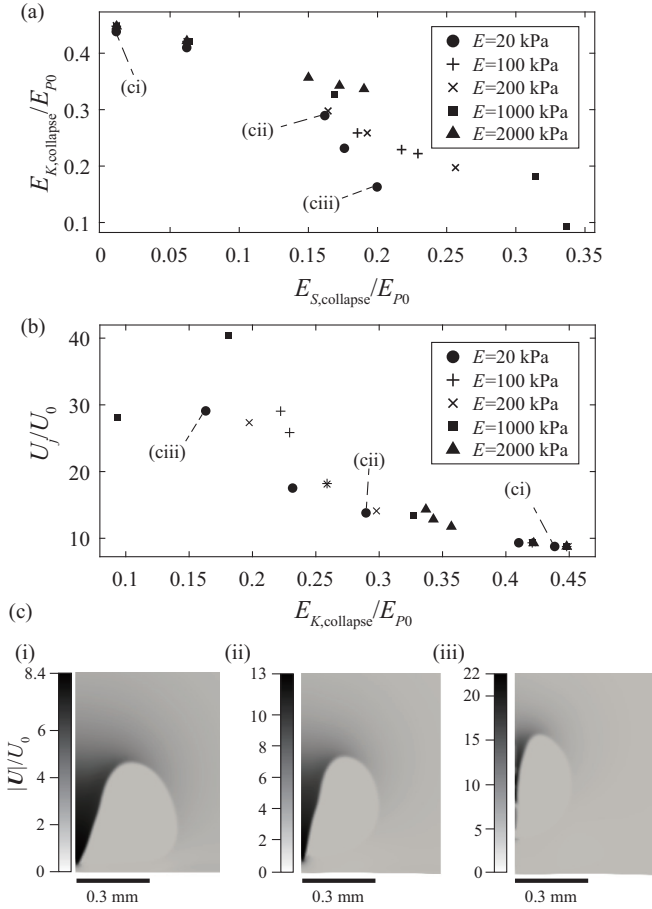


FIG. 15. (a) Relationship between fluid kinetic energy at bubble collapse time, $E_{K,\text{collapse}}$, and total energy transferred to the solid up to collapse time, $E_{S,\text{collapse}}$, for viscoelastic solids. (b) Relationship between liquid jet speed U_j and $E_{K,\text{collapse}}$. (c) Contours of velocity magnitude for viscoelastic cases at bubble collapse time: (i) $E = 20$ kPa, $\eta = 1000$ Pa s; (ii) $E = 20$ kPa, $\eta = 10$ Pa s; (iii) $E = 20$ kPa, $\eta = 2$ Pa s. See Supplemental Material movie 2 for (c).

D. Impact of liquid jet on a solid surface

As a liquid jet with a high momentum impacts a solid surface, the surface rapidly deforms downwards, creating a crater near its center. Although the highly nonlinear behavior of the liquid jet makes it difficult to find consistent trends regarding its interaction with the solid, some notable features regarding the solid surface deserve to be reported. Upon the impact of the liquid jet, the responses of the elastic and viscoelastic solids are markedly different [Fig. 16]. In the figure, the profiles of the solid surface are drawn every $5 \mu\text{s}$ from the collapse time of the bubble to the end of the simulation ($t = 160 \mu\text{s}$). The elastic solids tend to deform smoothly over an extensive area around the impact zone [Figs. 16(a)–16(c)], while the deformation of the viscoelastic solids is more concentrated near the surface center [Figs. 16(d)–16(i)]. This tendency differs dramatically from that of the initial downward deformation phase of the surface mentioned in Sec. III A. In the initial downward deformation phase, the effect of the solid viscosity on the profile of the solid surface is minor, although the solid viscosity influences the degree of surface deformation [Fig. 4(b)].

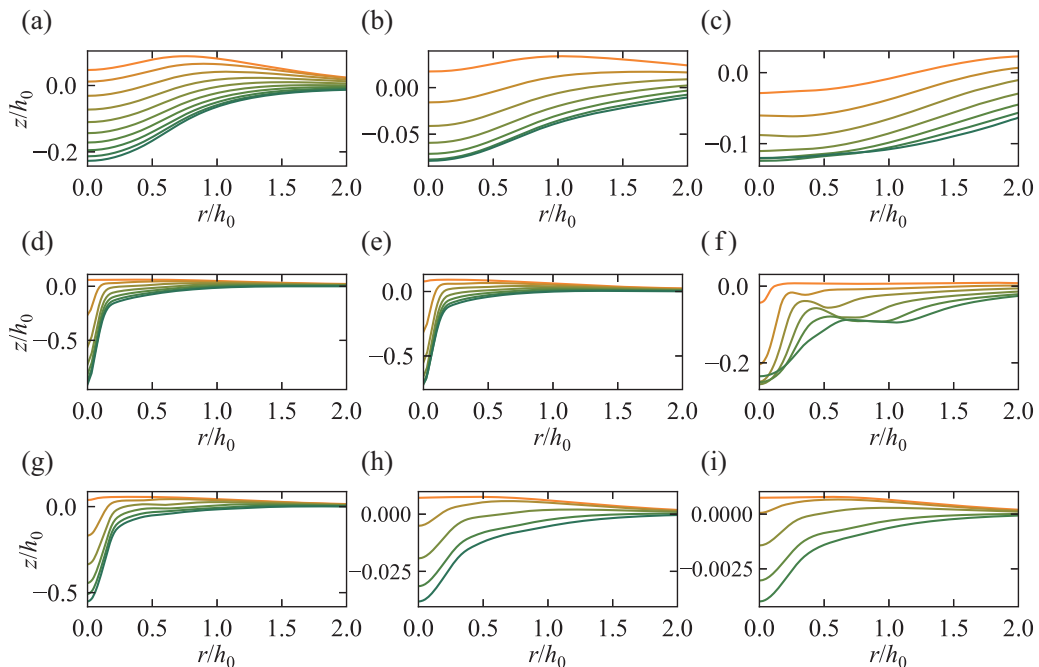


FIG. 16. Sequential profiles of solid surface after liquid jet impact for (a)–(c) purely elastic solids and (d)–(i) viscoelastic solids: (a) $E = 20$ kPa; (b) $E = 100$ kPa; (c) $E = 2000$ kPa; (d) $E = 20$ kPa, $\eta = 2$ Pa s; (e) $E = 100$ kPa, $\eta = 2$ Pa s; (f) $E = 2000$ kPa, $\eta = 2$ Pa s; (g) $E = 20$ kPa, $\eta = 5$ Pa s; (h) $E = 20$ kPa, $\eta = 100$ Pa s; (i) $E = 20$ kPa, $\eta = 1000$ Pa s. The profiles are captured every $5 \mu\text{s}$.

The liquid jet of the elastic cases creates a certain distance above the solid surface, while the liquid jet of the viscoelastic cases is formed closer to the solid surface (Fig. 11). Moreover, in the elastic solids, the jet is either directed away from the solid surface or split into two directions, depending on the elastic modulus. That is, the relative location and direction of the liquid jet generation strongly affects the profile of the surface. As the magnitude of the jet momentum varies nonlinearly with the elastic modulus, no correlation between the degree of surface deformation and the elastic modulus can be identified.

In contrast to the elastic solids [Figs. 16(a)–16(c)], a small solid viscosity creates a very narrow and deep crater under the same elastic modulus [Figs. 16(d)–16(f)]. When the liquid jet is formed closer to the solid surface and is directed towards the surface, a more concentrated deformation is induced. The crater becomes wider as the solid viscosity increases [Figs. 16(d), 16(g), 16(h), and 16(i)]. The width of the crater scales with the width of the liquid jet, as observed in a comparison of the liquid jet in Figs. 15(c*i*) and 15(c*iii*) and the corresponding surface deformations after jet impact in Figs. 16(i) and 16(d). Furthermore, the penetration depth of the surface decreases as the solid viscosity increases, which matches the trend of the initial downward deformation [Fig. 4(a)]. According to Fig. 12(a), the liquid jet speed U_j decreases with increasing solid viscosity. In summary, the increase in the solid viscosity contributes to shallower surface penetration in two ways: by inducing a slower liquid jet with low momentum and by making the solid itself respond more slowly to the jet impact.

In Fig. 16(f) ($E = 2000$ kPa, $\eta = 2$ Pa s, $De = 0.04$), a transverse surface wave with a small amplitude propagates outwards in the radial direction. This phenomenon is not observed in the other viscoelastic cases with lower elastic moduli and the same viscosity [Figs. 16(d) and 16(e)]. The Deborah number of this case is exceptionally small, so the viscoelastic solid behaves more like an elastic solid with weak attenuation of the surface wave [87]. In the purely elastic solid

[Figs. 16(a)–16(c)], actually no surface wave is observed because the liquid jet is not directed towards the surface and the surface deforms over an extensive area. However, the elastic solid with $E = 200$ kPa, which is not included in Fig. 16, induces a relatively large portion of the liquid jet to be directed towards the solid surface [Fig. 11(c)], thereby creating a narrow penetration in a concentrated area and resultant surface wave propagation.

We would like to mention that this paper has a limitation in accurately describing solid deformation during this stage. Our numerical method does not account for nonlinear deformations of the solid that may occur by the liquid jet. Moreover, it neglects the effect of viscous stress on solid deformation although the magnitude of wall shear stress at this jet impingement stage increases to approximately 10% of stagnation pressure. Further research is required to understand the influence of these factors on solid deformation. Nevertheless, the overall shapes of jet-induced solid deformation, which are reported in this paper, are expected to be similar to those of actual scenarios.

IV. CONCLUDING REMARKS

We have investigated the dynamics of a bubble and the deformation of a nearby viscoelastic solid in four sequential stages, from the expansion of the bubble to the impingement of a liquid jet onto the solid surface. Compared with a purely elastic solid, the viscosity of the viscoelastic solid dramatically changes its response to bubble expansion and collapse, which in turn affects the behaviors of the bubble and liquid jet. The Deborah number has been used to characterize the interactions between the bubble and viscoelastic solid. As the Deborah number increases, the response of the solid becomes slower and weaker. This causes the parameters relevant to the bubble (such as the liquid jet speed) and the parameters relevant to the solid (such as the maximum displacement) to converge to the values of the rigid solid case. Some part of the energy in the fluid domain is transferred to the solid domain through deformation, leading to the decrease in the bubble potential energy at the instant of maximum expansion, and the amount of energy transfer is inversely related with the maximum bubble radius. As the solid viscosity decreases, the rebounding speed of the solid boundary grows, altering the shape of the contracting bubble. With the smaller solid viscosity, the stronger pressure anisotropy around the contracting bubble contributes to a faster jet speed, and the jet speed can be further enhanced by the formation of a narrow jet region, although the jet kinetic energy may drop due to the greater amount of energy transferred to the solid domain. The solid viscosity remarkably changes the penetration shape formed on the solid surface upon the impingement of the liquid jet. With a small viscosity, the liquid jet is concentrated near the solid center, creating a sharp and deep crater.

This paper has primarily focused on revealing the effects of solid viscoelasticity for given initial bubble conditions. To further validate the characterization of bubble-viscoelastic solid interactions using the Deborah number, different initial conditions for the bubble should be comprehensively examined. Future study requires diverse initial pressures and stand-off parameters for the bubble and new viscoelastic models, such as the Maxwell model, to elaborate on the physical mechanisms underlying the complex interactions between a viscoelastic solid, a gas bubble, and a surrounding liquid.

ACKNOWLEDGMENTS

This research was supported by the Basic Science Research Program through the National Research Foundation of Korea (NRF) funded by the Ministry of Science and ICT (NRF-2020R1A2C2102232) and by a Korea Institute for Advancement of Technology (KIAT) grant funded by the Korea Government (MOTIE) (No. P0017006, The Competency Development Program for Industry Specialist).

The authors report no conflict of interest.

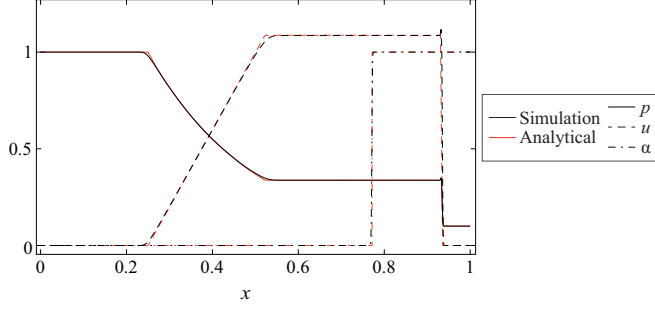


FIG. 17. Comparison of pressure p , velocity u , and volume fraction α fields at $t = 0.25$ in one-dimensional shock tube problem: Simulation results (black lines) and analytical solutions from Miller *et al.* [71] (red lines).

APPENDIX A: VALIDATION OF SHOCK WAVE PROPAGATION

The capability of the fluid solver to resolve shock waves is validated by comparing results of a two-phase shock-tube problem with its analytical solutions. The specific configuration of the problem is set identical to that of Miller *et al.* [71]. The computational domain is one-dimensional and has a length of 1, with an array of 1000 cells. The time step is fixed to $\Delta t = 10^{-4}$. Initial conditions are set to be

$$p(x, 0) = \begin{cases} 1.0, & x < 0.5 \\ 0.1, & x > 0.5 \end{cases}, \quad u(x, 0) = 0, \quad \alpha(x, 0) = \begin{cases} 1, & x < 0.5 \\ 0, & x > 0.5 \end{cases}, \quad (\text{A1})$$

where p , u , and α represent the pressure, velocity, and volume fraction, respectively. The polytropic equation of state for the gas is

$$\frac{p}{\rho^\gamma} = a_c, \quad (\text{A2})$$

where $\gamma = 1.25$ and $a_c = 1.35$. For the liquid state, the isothermal equation of state is used as

$$\rho - \rho_0 = \psi(p - p_0), \quad (\text{A3})$$

where $\rho_0 = 0$, $p_0 = 0$, and $\psi = 1$. Pressure, velocity, and volume fraction fields at $t = 0.25$ of our simulation results are compared with those of analytical results in Fig. 17, confirming that the fluid solver can accurately capture shock-wave dynamics.

APPENDIX B: VALIDATION OF THE SOLID SOLVER AND THE KELVIN-VOIGT MODEL

The solid solver and the KelvinVoigt model used for the finite element method are validated by comparing a viscoelastic behavior with that of an analytical solution. In the absence of a fluid domain, a solid domain with the size and grid layout identical to the main simulation is exposed to a uniform compressive stress of 100 kPa along the axial direction from $t = 0 - 1.0$ s. Unlike the main simulation, only the bottom surface of the solid is fixed while the side surface is free to deform. Five different values of the viscosity, $\eta = [5, 10, 50, 100, 1000]$ Pa s, are used with the fixed values of the elastic modulus and Poisson's ratio ($E = 1000$ kPa, $\nu = 0.4$).

To obtain the analytical solution, the axial stress–strain relation for a Kelvin-Voigt solid under a uniaxial stress is obtained from Eq. (1):

$$\sigma_{zz} = [\lambda(1 - 2\nu) + 2G]\varepsilon_{zz} + [\lambda(1 - 2\nu)\tau_\lambda + 2G\tau_S]\dot{\varepsilon}_{zz}. \quad (\text{B1})$$

In Eq. (B1), the coefficient of the strain rate corresponds to the extensional viscosity η_E :

$$\eta_E = \lambda(1 - 2\nu)\tau_\lambda + 2G\tau_S. \quad (\text{B2})$$

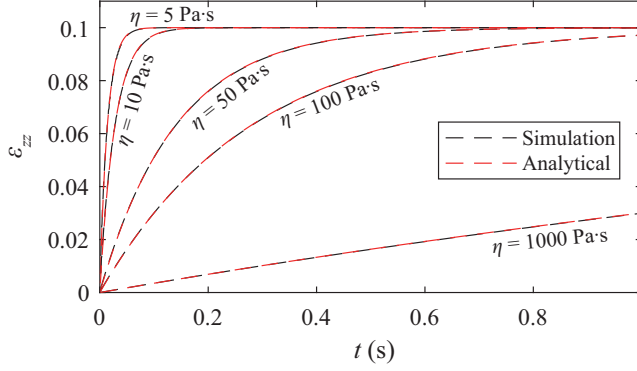


FIG. 18. Comparison of temporal variations in normal strain between simulation results (black dashed lines) and analytical solution (red dashed lines) for five different viscosities.

Using Eq. (2) and Eq. (B2), Eq. (B1) is simply rewritten as

$$\sigma_{zz} = E\varepsilon_{zz} + \eta_E \dot{\varepsilon}_{zz}. \quad (\text{B3})$$

The axial strain of the Kelvin-Voigt solid is obtained as a function of time by solving Eq. (B3):

$$\varepsilon_{zz}(t) = \frac{\sigma_{zz}}{E} (1 - e^{-Et/\eta_E}). \quad (\text{B4})$$

Here, the characteristic time of the Kelvin-Voigt solid under a uniaxial stress is η_E/E . Since the value of η_E is unknown, it needs to be changed into the form which consists of known variables such as G and η . According to Linn [65], η_E is defined as

$$\eta_E = \zeta(1 - 2\nu)^2 + \frac{4}{3}\eta(1 + \nu)^2, \quad (\text{B5})$$

where ζ is the bulk viscosity. ζ is also expressed as $\zeta = \frac{2+2\nu}{3-6\nu}\eta$ [88]. After substituting this into Eq. (B5) and conducting some algebraic procedures, it comes to the conclusion that

$$\frac{\eta_E}{E} = \frac{\eta}{G}. \quad (\text{B6})$$

This shows that the extensional characteristic time $\tau_E (= \eta_E/E)$ is identical to the characteristic time $\tau_S (= \eta/G)$ defined in Sec. II A. It should be noted that Eq. (B6) only holds for a Kelvin-Voigt solid under a uniaxial stress.

Using Eq. (B6), the analytical solution Eq. (B4) is expressed as

$$\varepsilon_{zz}(t) = \frac{\sigma_{zz}}{E} (1 - e^{-Gt/\eta}) = \frac{\sigma_{zz}}{E} (1 - e^{-Et/2(1+\nu)\eta}). \quad (\text{B7})$$

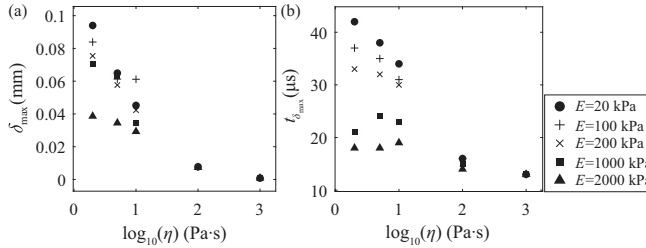


FIG. 19. (a) Maximum displacement δ_{\max} and (b) time at maximum displacement $t_{\delta_{\max}}$ for viscoelastic solids with different properties.

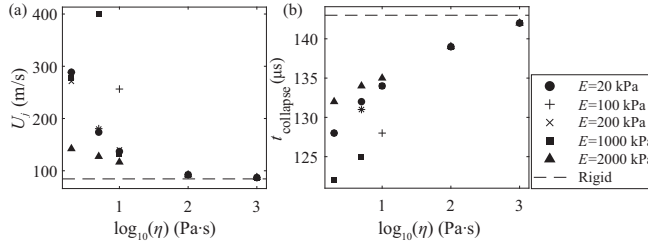


FIG. 20. (a) Liquid jet speed U_j and (b) bubble collapse time t_{collapse} for different solid properties. The dashed horizontal line denotes the value for the rigid solid case.

According to Fig. 18, our numerical method accurately computes the viscoelastic deformation of the solid over a wide range of η .

APPENDIX C: RESULTS PLOTTED WITH DIMENSIONAL PARAMETERS

Figure 19 presents the maximum displacement δ_{max} of the solid and the corresponding time $t_{\delta_{\text{max}}}$ with respect to the solid viscosity η . For each value of the elastic modulus E , both δ_{max} and $t_{\delta_{\text{max}}}$ tend to decrease as η increases, having relatively greater variations with respect to E at a given De compared with Fig. 6. For a given value of η , the solid generally undergoes greater deformation at smaller values of E , and the deformation process accordingly takes more time.

For a given elastic modulus E , as the solid viscosity η increases, the jet speed U_j decreases sharply and converges to that of the rigid solid case [Fig. 20(a)]. Figure 20(b) shows that t_{collapse} increases with η and approaches that of the rigid solid. The convergence of U_j and t_{collapse} to values corresponding to the rigid solid with increasing η is consistent with the converging tendency of δ_{max} and $t_{\delta_{\text{max}}}$ with increasing η , which is depicted in Fig. 19.

-
- [1] Y. Tomita and A. Shima, Mechanisms of impulsive pressure generation and damage pit formation by bubble collapse, *J. Fluid Mech.* **169**, 535 (1986).
 - [2] P. Cui, A. Zhang, S. Wang, and B. C. Khoo, Ice breaking by a collapsing bubble, *J. Fluid Mech.* **841**, 287 (2018).
 - [3] M. Dular, T. Pozar, J. Zevnik, and R. Petkovšek, High speed observation of damage created by a collapse of a single cavitation bubble, *Wear* **418–419**, 13 (2019).
 - [4] R. E. A. Arndt, Cavitation in fluid machinery and hydraulic structures, *Annu. Rev. Fluid Mech.* **13**, 273 (1981).
 - [5] A. Philipp and W. Lauterborn, Cavitation erosion by single laser-produced bubbles, *J. Fluid Mech.* **361**, 75 (1998).
 - [6] J. C. Isselin, A. P. Alloncle, and M. Autric, On laser induced single bubble near a solid boundary: Contribution to the understanding of erosion phenomena, *J. Appl. Phys.* **84**, 5766 (1998).
 - [7] S. Hattori, T. Hirose, and K. Sugiyama, Prediction method for cavitation erosion based on measurement of bubble collapse impact loads, *Wear* **269**, 507 (2010).
 - [8] K. H. Kim, G. Chahine, J. P. Franc, and A. Karimi, *Advanced Experimental and Numerical Techniques for Cavitation Erosion Prediction* (Springer, Dordrecht, Netherlands, 2014).
 - [9] D. Kim and D. Kim, Underwater bubble collapse on a ridge-patterned structure, *Phys. Fluids* **32**, 053312 (2020).
 - [10] A. K. Krella, Cavitation erosion of monolayer pvd coatings—an influence of deposition technique on the degradation process, *Wear* **478–479**, 203762 (2021).

- [11] B. Liu and F. Ma, Erosion behavior of aluminum by an inclined cavitating jet, *Wear* **474–475**, 203751 (2021).
- [12] T. Trummler, S. J. Schmidt, and N. A. Adams, Numerical prediction of erosion due to a cavitating jet, *Wear* **498–499**, 204304 (2022).
- [13] E. A. Brujan, The role of cavitation microjets in the therapeutic applications of ultrasound, *Ultrasound Med. Biol.* **30**, 381 (2004).
- [14] C. D. Ohl, M. Arora, R. Ikink, N. de Jong, M. Versluis, M. Delius, and D. Lohse, Sonoporation from jetting cavitation bubbles, *Biophys. J.* **91**, 4285 (2006).
- [15] S. Hernot and A. L. Klibanov, Microbubbles in ultrasound-triggered drug and gene delivery, *Adv. Drug Deliv. Rev.* **60**, 1153 (2008).
- [16] A. Azagury, L. Khoury, G. Enden, and J. Kost, Ultrasound mediated transdermal drug delivery, *Adv. Drug Deliv. Rev.* **72**, 127 (2014).
- [17] A. Jamburidze, A. Huerre, D. Baresch, V. Poulichet, M. D. Corato, and V. Garbin, Nanoparticle-coated microbubbles for combined ultrasound imaging and drug delivery, *Langmuir* **35**, 10087 (2019).
- [18] M. Bok, Z. J. Zhao, S. Jeon, J. H. Jeong, and E. Lim, Ultrasonically and iontophoretically enhanced drug-delivery system based on dissolving microneedle patches, *Sci. Rep.* **10**, 2027 (2020).
- [19] K. Kooiman, S. Roovers, S. A. G. Langeveld, R. T. Kleven, H. Dewitte, M. A. O'Reilly, J. M. Escoffre, A. Bouakaz, M. D. Verweij, K. Hynynen, I. Lentacker, E. Stride, and C. K. Holland, Ultrasound-responsive cavitation nuclei for therapy and drug delivery, *Ultrasound Med. Biol.* **46**, 1296 (2020).
- [20] B. R. Ringeisen, C. M. Othon, J. A. Barron, D. Young, and B. J. Spargo, Jet-based methods to print living cells, *Biotechnol. J.* **1**, 930 (2006).
- [21] D. Lohse, Bubble puzzles: From fundamentals to applications, *Phys. Rev. Fluids* **3**, 110504 (2018).
- [22] E. Mahravan and D. Kim, Bubble collapse and jet formation inside a liquid film, *Phys. Fluids* **33**, 112102 (2021).
- [23] G. L. Chahine, A. Kapahi, J. K. Choi, and C. T. Hsiao, Modeling of surface cleaning by cavitation bubble dynamics and collapse, *Ultrason. Sonochem.* **29**, 528 (2016).
- [24] F. Reuter and R. Mettin, Mechanisms of single bubble cleaning, *Ultrason. Sonochem.* **29**, 550 (2016).
- [25] T. Yamashita and K. Ando, Low-intensity ultrasound induced cavitation and streaming in oxygen-supersaturated water: Role of cavitation bubbles as physical cleaning agents, *Ultrason. Sonochem.* **52**, 268 (2019).
- [26] C. Song and W. Cui, Review of underwater ship hull cleaning technologies, *J. Mar. Sci. Appl.* **19**, 415 (2020).
- [27] J. R. Blake, The Kelvin impulse: Application to cavitation bubble dynamics, *J. Aust. Math. Soc. Ser. B* **30**, 127 (1988).
- [28] Q. X. Wang, K. S. Yeo, B. C. Khoo, and K. Y. Lam, Nonlinear interaction between gas bubble and free surface, *Comput. Fluids* **25**, 607 (1996).
- [29] L. Duchemin, S. Popinet, C. Josserand, and S. Zaleski, Jet formation in bubbles bursting at a free surface, *Phys. Fluids* **14**, 3000 (2002).
- [30] S. Zhang, S. P. Wang, and A. M. Zhang, Experimental study on the interaction between bubble and free surface using a high-voltage spark generator, *Phys. Fluids* **28**, 032109 (2016).
- [31] P. Koukouvinis, M. Gavaises, O. Supponen, and M. Farhat, Simulation of bubble expansion and collapse in the vicinity of a free surface, *Phys. Fluids* **28**, 052103 (2016).
- [32] W. Lauterborn and H. Bolle, Experimental investigations of cavitation-bubble collapse in the neighborhood of a solid boundary, *J. Fluid Mech.* **72**, 391 (1975).
- [33] S. Zhang, J. H. Duncan, and G. L. Chahine, The final stage of the collapse of a cavitation bubble near a rigid wall, *J. Fluid Mech.* **257**, 147 (1993).
- [34] E. A. Brujan, G. S. Keen, A. Vogel, and J. R. Blake, The final stage of the collapse of a cavitation bubble close to a rigid boundary, *Phys. Fluids* **14**, 85 (2002).
- [35] E. Johnsen and T. Colonius, Numerical simulations of non-spherical bubble collapse, *J. Fluid Mech.* **629**, 231 (2009).
- [36] E. A. Brujan, Jets from pulsed-ultrasound-induced cavitation bubbles near a rigid boundary, *J. Phys. D: Appl. Phys.* **50**, 215302 (2017).

- [37] Q. Zeng, S. R. Gonzalez-Avila, R. Dijkink, P. Koukouvinis, M. Gavaises, and C. D. Ohl, Wall shear stress from jetting cavitation bubbles, *J. Fluid Mech.* **846**, 341 (2018).
- [38] O. Supponen, D. Obreschkow, M. Tinguely, P. Kobel, N. Dorsaz, and M. Farhat, Scaling laws for jets of single cavitation bubbles, *J. Fluid Mech.* **802**, 263 (2016).
- [39] T. Trummer, S. H. Bryngelson, K. Schmidmayer, S. J. Schmidt, T. Colonius, and N. A. Adams, Near-surface dynamics of a gas bubble collapsing above a crevice, *J. Fluid Mech.* **899**, A16 (2020).
- [40] M. Rodriguez Jr, S. A. Beig, C. N. Barbier, and E. Johnsen, Dynamics of an internally collapsing gas bubble between two parallel, rigid walls, *J. Fluid Mech.* **946**, A43 (2022).
- [41] Y. Tomita, P. B. Robinson, R. P. Tong, and J. R. Blake, Growth and collapse of cavitation bubbles near a curved rigid boundary, *J. Fluid Mech.* **466**, 259 (2002).
- [42] E. Kadivar, O. Moctar, and H. J. Sagar, Experimental study of the influence of mesoscale surface structuring on single bubble dynamics, *Ocean Eng.* **260**, 111892 (2022).
- [43] X. Ma, B. Huang, X. Zhao, Y. Wang, Q. Chang, S. Qiu, and X. Fu, Comparisons of spark-charge bubble dynamics near the elastic and rigid boundaries, *Ultrason. Sonochem.* **43**, 80 (2018).
- [44] Y. Zhai, W. Xu, J. Luo, and J. Li, Experimental study on the characteristics of microjets and shock waves of cavitation bubbles near elastic boundaries, *Ocean Eng.* **257**, 111664 (2022).
- [45] E. A. Brujan, K. Nahen, P. Schmidt, and A. Vogel, Dynamics of laser-induced cavitation bubbles near an elastic boundary, *J. Fluid Mech.* **433**, 251 (2001).
- [46] E. Klaseboer and B. C. Khoo, An oscillating bubble near an elastic material, *J. Appl. Phys.* **96**, 5808 (2004).
- [47] S. W. Ohl, E. Klaseboer, and B. C. Khoo, The dynamics of a non-equilibrium bubble near bio-materials, *Phys. Med. Biol.* **54**, 6313 (2009).
- [48] M. T. Shervani-Tabar, A. H. Aghdam, B. C. Khoo, V. Farhangmehr, and B. Farzaneh, Numerical analysis of a cavitation bubble in the vicinity of an elastic membrane, *Fluid Dyn. Res.* **45**, 055503 (2013).
- [49] S. W. Gong, S. W. Ohl, E. Klaseboer, and B. C. Khoo, Interaction of a spark-generated bubble with a two-layered composite beam, *J. Fluids Struct.* **76**, 336 (2018).
- [50] T. Zhao, X. Zhao, X. Ma, and B. Huang, Numerical investigations of the bubble collapse near an elastic plate, *J. Fluids Struct.* **106**, 103372 (2021).
- [51] E. A. Brujan, K. Nahen, P. Schmidt, and A. Vogel, Dynamics of laser-induced cavitation bubbles near elastic boundaries: Influence of the elastic modulus, *J. Fluid Mech.* **433**, 283 (2001).
- [52] B. Dollet, P. Marmottant, and V. Garbin, Bubble dynamics in soft and biological matter, *Annu. Rev. Fluid Mech.* **51**, 331 (2019).
- [53] L. Mancia, E. Vlaisavljevich, N. Yousefi, M. Rodriguez, T. J. Ziemlewicz, F. T. Lee, D. Henann, C. Franck, Z. Xu, and E. Johnsen, Modeling tissue-selective cavitation damage, *Phys. Med. Biol.* **64**, 225001 (2019).
- [54] A. Maccabi, A. Shin, N. K. Namiri, N. Bajwa, M. S. John, Z. D. Taylor, W. Grundfest, and G. N. Saddik, Quantitative characterization of viscoelastic behavior in tissue-mimicking phantoms and *ex vivo* animal tissues, *PLoS ONE* **13**, e0191919 (2018).
- [55] L. G. Tolley and R. G. Craig, Viscoelastic properties of elastomeric impression materials: Polysulphide, silicone and polyether rubbers, *J. Oral Rehabil.* **5**, 121 (1978).
- [56] L. Bazli, A. Khavandi, M. A. Boutorabi, and M. Karrabi, Morphology and viscoelastic behavior of silicone rubber/EPDM/Cloisite 15A nanocomposites based on Maxwell model, *Iran Polym. J.* **25**, 907 (2016).
- [57] A. Shima, Y. Tomita, D. C. Gibson, and J. R. Blake, The growth and collapse of cavitation bubbles near composite surfaces, *J. Fluid Mech.* **203**, 199 (1989).
- [58] J. H. Duncan, C. D. Milligan, and S. Zhang, On the interaction between a bubble and a submerged compliant structure, *J. Sound Vib.* **197**, 17 (1996).
- [59] S. W. Gong and E. Klaseboer, Interaction between collapsing bubble and viscoelastic solid: Numerical modelling and simulation, *Appl. Math. Model.* **40**, 4746 (2016).
- [60] M. Rodriguez, Numerical simulations of bubble dynamics near viscoelastic media, Ph.D. thesis, University of Michigan, 2018.
- [61] L. A. Frizzel, E. L. Carstensen, and J. F. Dyro, Shear properties of mammalian tissues at low megahertz frequencies, *J. Acoust. Soc. Am.* **60**, 1409 (1976).

- [62] E. L. Madsen, H. J. Sathoff, and H. J. Zagzebski, Ultrasonic shear wave properties of soft tissues and tissuelike materials, *J. Acoust. Soc. Am.* **74**, 1346 (1983).
- [63] T. Takebe, M. Enomura, E. Yoshizawa, M. Kimura, H. Koike, Y. Ueno, T. Matsuzaki, T. Yamazaki, T. Toyohara, K. Osafune, H. Nakauchi, H. Y. Yoshikawa, and H. Taniguchi, Vascularized and complex organ buds from diverse tissues via mesenchymal cell-driven condensation, *Cell Stem Cell* **16**, 556 (2015).
- [64] J. Lemaitre and J. Chaboche, *Mechanics of Solid Materials* (Cambridge University Press, Cambridge, 1990).
- [65] J. Linn, Derivation of a viscoelastic constitutive model of Kelvin-Voigt type for Cosserat rods, *Mech. Sci.* **4**, 79 (2013).
- [66] M. Qaisar, Attenuation properties of viscoelastic material, *Pure Appl. Geophys.* **131**, 703 (1989).
- [67] G. Constantinides, Z. I. Klacioglu, M. McFarland, J. F. Smith, and K. J. V. Vliet, Probing mechanical properties of fully hydrated gels and biological tissues, *J. Biomech.* **41**, 3285 (2008).
- [68] N. Nikolaev, T. Müller, D. J. Williams, and Y. Liu, Changes in the stiffness of human mesenchymal stem cells with the progress of cell death as measured by atomic force microscopy, *J. Biomech.* **47**, 625 (2014).
- [69] S. N. Sundaresh, J. D. Finan, B. S. Elkin, A. V. Basilio, G. M. McKhann, and B. M. III, Region-dependent viscoelastic properties of human brain tissue under large deformations, *Ann. Biomed. Eng.* **50**, 1452 (2022).
- [70] H. G. Weller, G. Tabor, H. Jasak, and C. Fureby, A tensorial approach to computational continuum mechanics using object-oriented techniques, *Comput. Phys.* **12**, 620 (1998).
- [71] S. T. Miller, H. Jasak, D. A. Boger, E. G. Paterson, and A. Nedungadi, A pressure-based, compressible, two-phase flow finite volume method for underwater explosions, *Comput. Fluids* **87**, 132 (2013).
- [72] M. Koch, C. Lechner, F. Reuter, K. Köhler, R. Mettin, and W. Lauterborn, Numerical modeling of laser generated cavitation bubbles with the finite volume and volume of fluid method, using OpenFOAM, *Comput. Fluids* **126**, 71 (2016).
- [73] E. Berberović, N. P. van Hinsberg, S. Jakirlić, I. V. Roisman, and C. Tropea, Drop impact onto a liquid layer of finite thickness: Dynamics of the cavity evolution, *Phys. Rev. E* **79**, 036306 (2009).
- [74] J. U. Brackbill, D. B. Kothe, and C. Zemach, A continuum method for modeling surface tension, *J. Comput. Phys.* **100**, 335 (1992).
- [75] K. Kobayashi, T. Nagayama, M. Watanabe, H. Fujii, and M. Kon, Molecular gas dynamics analysis on condensation coefficient of vapour during gas–vapour bubble collapse, *J. Fluid Mech.* **856**, 1045 (2018).
- [76] R. I. Issa, Solution of the implicitly discretised fluid flow equations by operator-splitting, *J. Comput. Phys.* **62**, 40 (1986).
- [77] A. Vogel and W. Lauterborn, Acoustic transient generation by laser-produced cavitation bubbles near solid boundaries, *J. Acoust. Soc. Am.* **84**, 719 (1988).
- [78] G. Dhondt, *The Finite Element Method for Three-Dimensional Thermomechanical Applications* (Wiley, West Sussex, UK, 2004).
- [79] H. J. Bungartz, F. Lindner, B. Gatzhammer, M. Mehl, K. Scheufele, A. Shukaev, and B. Uekermann, preCICE - A fully parallel library for multi-physics surface coupling, *Comput. Fluids* **141**, 250 (2016).
- [80] Q. Zeng, H. An, and C. Ohl, Wall shear stress from jetting cavitation bubbles: Influence of the stand-off distance and liquid viscosity, *J. Fluid Mech.* **932**, A14 (2022).
- [81] H. A. Barnes, J. F. Hutton, and K. Walters, *An Introduction to Rheology* (Elsevier, Amsterdam, 1989).
- [82] F. R. Gilmore, *The Growth or Collapse of a Spherical Bubble in a Viscous Compressible Liquid* (California Institute of Technology, 1952).
- [83] Q. X. Wang, Local energy of a bubble system and its loss due to acoustic radiation, *J. Fluid Mech.* **797**, 201 (2016).
- [84] See Supplemental Material at <http://link.aps.org/supplemental/10.1103/PhysRevFluids.9.043603> for the animated version of Fig. 11.
- [85] A. Kapahi, C. T. Hsiao, and G. L. Chahine, Shock-induced bubble collapse versus Rayleigh collapse, *J. Phys.: Conf. Ser.* **656**, 012128 (2015).
- [86] H. Xue, F. Shan, X. Guo, J. Tu, and D. Zhang, Cavitation bubble collapse near a curved wall by the multiple-relaxation-time Shan-Chen lattice Boltzmann model, *Chin. Phys. Lett.* **34**, 084301 (2017).

- [87] J. M. Carcione, F. Poletto, and D. Gei, 3-D wave simulation in an elastic media using the Kelvin-Voigt constitutive equation, *J. Comput. Phys.* **196**, 282 (2004).
- [88] R. K. Bordia and G. W. Scherer, On constrained sintering–II. Comparison of constitutive models, *Acta Metall.* **36**, 2399 (1988).